In mice and humans, brain microvascular contractility matures postnatally

Leila Slaoui, Alice Gilbert, Armelle Rancillac, Barbara Delaunay-Piednoir, Audrey Chagnot, Quentin Gerard, Gaëlle Letort, Philippe Mailly, Noémie Robil, Antoinette Gelot, et al.

In mice and humans, brain microvascular contractility matures postnatally

Brain microvessel post-natal maturation

Leila Slaoui[1]*, Alice Gilbert[1]*, Armelle Rancillac[1], Barbara Delaunay-Piednoir [1], Audrey Chagnot [2], Quentin Gerard [2], Gaëlle Letort [1], Philippe Mailly[1], Noémie Robil [3], Antoinette Gelot [4], Mathilde Lefebvre [5], Maryline Favier [6], Karine Dias [7], Laurent Jourdren[7], Laetitia Federici [8], Sylvain Auvity [8,9], Salvatore Cisternino [8,9], Denis Vivien [2,10], Martine Cohen-Salmon[1]** and Anne-Cécile Boulay[1]**

[1] Center for Interdisciplinary Research in Biology (CIRB), Collège de France, CNRS, INSERM, Université PSL, Paris, France.

[2] Normandie University, UNICAEN, INSERM UMR-S U1237, Physiopathology and Imaging of Neurological Disorders (PhIND), GIP Cyceron, Institute Blood and Brain @ Caen-Normandie (BB@C), 14000 Caen, France.

[3] Genosplice, Paris, France.

[4] Service d'anatomie et cytologie pathologie, Assistance Publique – Hôpitaux de Paris, Hôpital Armand Trousseau, Paris, France.

[5] Service de foetopathologie, Centre hospitalier régional d'Orleans, France.

[6] HistIM Facility, Institut Cochin, Paris, France.

[7] GenomiqueENS, Institut de Biologie de l'ENS (IBENS), Département de biologie, École normale supérieure, CNRS, INSERM, Université PSL, 75005 Paris, France

[8] Optimisation Thérapeutique en Neuropsychopharmacologie, INSERM, Université de Paris, Paris, France.

[9] Service Pharmacie, Assistance Publique – Hôpitaux de Paris, Hôpital Universitaire – Necker – Enfants Malades, Paris, France.

[10] Department of clinical research, Caen-Normandie University Hospital, CHU, Avenue de la côte de Nacre, Caen, France.

* joint first authors

** joint last authors

Correspondence: martine.cohen-salmon@college-de-france.fr

Abstract

Although great efforts to characterize the embryonic phase of brain microvascular system development have been made, its postnatal maturation has barely been described. Here, we compared the molecular and functional properties of brain vascular cells on postnatal day (P)5 vs. P15, via a transcriptomic analysis of purified mouse cortical microvessels (MVs) and the identification of vascular-cell-type-specific or -preferentially expressed transcripts. We found that endothelial cells (EC), vascular smooth muscle cells (VSMC) and fibroblasts (FB) follow specific molecular maturation programs over this time period. Focusing on VSMCs, we showed that arteriolar VSMC network expands and becomes contractile resulting in a greater cerebral blood flow (CBF), with heterogenous developmental trajectories within cortical regions. Samples of human brain cortex showed the same postnatal maturation process. Thus, the postnatal phase is a critical period during which arteriolar VSMC contractility required for vessel tone and brain perfusion is acquired and mature.

Keywords: Brain microvessels; Postnatal development; Vascular smooth muscle cell; microvessel contractility; Cerebral blood flow

Introduction

The brain's extremely dense microvascular system sustains the neurons' high metabolic demand by providing the cells with a regulated flow of blood and physically and functionally sheltering them from harmful components in the blood. These microvessels form a complex, heterogeneous network. Penetrating arterioles ramify into a dense capillary tree that converges into venules and then veins. These microvessels are composed of endothelial cells (ECs) which form the vessel walls and constitute the BBB that separates the blood from the parenchyma in most areas of the brain. ECs are surrounded by mural cells (MCs), which include pericytes (PC) and vascular smooth muscle cells (VSMCs). VSMCs and PC are molecularly and functionally distinct and occupy different zones along the vascular arteriovenous axis. VSMCs locate to arterioles and venules and pericytes to capillaries (Hartmann et al. 2021; Lendahl et al. 2019; Attwell et al. 2016). Arteriolar VSMCs are contractile and control the vascular tone and blood perfusion (Rungta et al. 2018). VSMCs become progressively sparser as the vessels branch and are present as discrete, non-contractile cells in veins (Frosen and Joutel 2018). Like VSMCs, PCs form a continuum that ranges from contractile cells around pre-capillary arterioles and capillaries to a mesh of star-shaped, non-contractile cells on post-capillary venules (Hartmann et al. 2015). They regulate capillary dilation in response to neuronal activity (Hall et al. 2014);(Hartmann et al. 2021). They also control angiogenesis (Daneman et al. 2010) and display stem cell properties (Dore-Duffy 2008; Nakagomi et al. 2015). Lastly, perivascular fibroblasts (FB) are present around vessels other than capillaries (Saunders et al. 2018; Vanlandewijck et al. 2018);(Dorrier et al. 2022). The FBs are highly heterogeneous and display various functions such as extracellular matrix (ECM) composition, blood vessel contractility, and immune control (Saunders et al. 2018; Manberg et al. 2021; Dorrier et al. 2022).

In rodents, the brain's blood vessels start to develop on or around embryonic day (E) 9. Firstly, ECs from a vascular plexus formed by mesodermal angioblasts, invade the neuroectoderm and form intraneural vessels (Coelho-Santos et al. 2021; Coelho-Santos and Shih 2020). They start expressing junctional proteins as early as they enter the brain parenchyma (Ben-Zvi and Liebner 2021). This angiogenic phase is followed by a differentiation phase around E15, during which pericytes originating both from mesoderm and neural crest (Wang 2015) are recruited to the endothelial surface. They induce EC's BBB properties such as low transcytosis, reduced paracellular transport and increased transcellular transport (Hellstrom et al. 1999; Daneman et al. 2010). Interestingly, a second wave of angiogenesis, vascular remodeling and BBB maturation occurs postnatally (Coelho-Santos et al. 2021; Coelho-Santos and Shih 2020), suggesting that angiogenesis and BBB genesis are interlinked. Much less is known about

the development of other vascular cells in the brain. In particular, the exact time course of VSMCs contractile differentiation remains unclear. A recent report described MC progenitors resembling pericytes differentiating postnatally into arterial/arteriolar VSMCs (Ando et al. 2022). Lastly, FBs have been shown to appear at the meningeal level around E12 while perivascular parenchymal FBs would be recruited only in the first 3 weeks after birth (Bonney et al. 2022).

To progress in the characterization and understanding of the molecular bases and functional consequences of the brain vascular system postnatal maturation, we combined here transcriptomic, biochemical, histochemical and functional assessments. We characterized the brain's microvascular compartment during postnatal development in mice and humans. Our results revealed that vascular cells follow a specific maturation program after birth. Focusing on VSMCs, we showed that this maturation results in the acquisition of VSMC contractility and cerebral perfusion.

Material and Methods

Animal experiments and ethical approval

Mice were purchased from Janvier Labs (Le Genest-Saint-Isle, France) and kept in pathogen-free conditions. All animal experiments were carried out in compliance with (i) the European Directive 2010/63/EU on the protection of animals used for scientific purposes and (ii) the guidelines issued by the French National Animal Care and Use Committee (reference: 2013/118). The study was also approved by the French Ministry for Research and Higher Education's institutional review board. No gender distinction was made. All studies were performed on swiss mice except *ex vivo* VSMC contractility tests that were done on C57BL6 mice.

Microvessel (MV) purification

MVs were purified from dorsal cortex (Fig. 1 and 2), dorsal and lateral cortex (Fig. 5) or whole brain (for other experiments), as described previously (Boulay et al. 2015). Briefly, brains were resuspended in HBSS/HEPES using an automated douncer. After a first centrifugation at 2000 g for 10 min, the pellet was resuspended in HBSS/Dextran 18% and centrifuged at 4000 g for 15 min to separate myelin from the vessels. This new pellet contained the brain vessels. It was resuspend in HBSS/BSA 1%. Filtration on a 100 µm-mesh filter allowed to remove large arteries and veins. The eluate was then filtrated on a 20 µm-mesh filter. MVs retained on the filter consisted in arterioles, venules and capillaries.

RNA sequencing and analysis

Total mRNA was extracted from purified cortical MVs on P5 or P15, using the RNeasy Lipid Tissue Kit (Qiagen, Hilden, Germany). Ten ng of total RNA were amplified and converted into cDNA using a SMART-Seq v4 Ultra Low Input RNA Kit (Clontech). Next, an average of 150 pg of amplified cDNA per library were processed with a Nextera XT DNA Kit (Illumina). Libraries were multiplexed on two high-output flow cells and sequenced (using 75 bp reads) on a NextSeq 500 device (Illumina). The mean ± standard deviation (SD) number of reads meeting the Illumina quality criterion was 48 ± 5 million per sample. The RNA-seq gene expression data and raw fastq files are available on the GEO repository (www.ncbi.nlm.nih.gov/geo/) under the accession number GSE173844. The RNA-Seq data were analyzed using GenoSplice technology (www.genosplice.com). Sequencing, data quality checks, read distribution checks (e.g. for potential ribosomal contamination), and insert size estimation were performed using FastQC, Picard-Tools, Samtools and rseqc. Reads were mapped onto the mm10 mouse genome

assembly using STARv2.4.0 (Dobin et al. 2013). The procedures for the gene expression regulation study have been described elsewhere (Noli et al. 2015). Briefly, for each gene present in the Mouse FAST DB v2018_1 annotation, we counted the reads aligning on constitutive regions (which are not prone to alternative splicing). Based on these counts, the level of differential gene expression was normalized using DESeq2 in R (v.3.2.5). Genes were considered to be expressed when their RPKM value was greater than 99% of the value for the background (intergenic region). Only genes annotated in Ensembl database and expressed in at least one of the two experimental conditions were analyzed further. Expression was considered to have changed significantly when the log2 fold change was ≥ 1 or ≤ -1 and padj was ≤ 0.05. Clusterings and heatmaps have been performed using "dist" and "hclust" functions in R, using Euclidean distance and Ward agglomeration method.

Pathway/Gene Ontology (GO) analysis

The GO analysis was performed using the DAVID functional annotation tool (version 6.8) (Huang da et al. 2009; Huang et al. 2007). Analysis for enriched KEGG pathways and REACTOME pathways were performed using WebGestaltR package, on databases from Mus Musculus organism (Wang et al. 2017). GO, KEGG and REACTOME terms and pathways were considered to be enriched if the following conditions were met: fold enrichment ≥ 2.0, uncorrected p-value ≤ 0.05, and minimum number of regulated genes in pathway/term ≥ 2.0. The analysis was performed three times: on all regulated genes, on upregulated genes only, and on downregulated genes only. The three sets of results were emerged to provide a single list. The transcription factor analysis was performed using mouse and human orthologs and the DAVID functional annotation Tool (version 6.8) (Huang da et al. 2009; Huang et al. 2007). The results were visualized using REViGO web tool (Supek et al. 2011).

Single-cell RNA-seq analysis

Raw reads from GEO datasets GSE99058 and GSE98816 were downloaded (He et al. 2016; Vanlandewijck et al. 2018). Seurat 3.1.1 was used to normalize unique molecular identifiers (Butler et al. 2018), using a global-scaling method with a scale factor of 10000 and log-transformation of the data. This was followed by a linear transformation scaling step, so as to avoid highly expressed genes with an excessively high weight in the downstream analysis. With the exception of PCs, cell types were grouped by their level of identity: fibroblasts (fibroblast-like type 1 and 2); ECs (types 1, 2 and 3 ECs, arterial ECs, venous ECs, and capillary ECs), and VSMCs (arteriolar SMCs, arterial SMCs, and venous SMCs). A transcript was considered to be specific or preferentially expressed in a given cell type when it was detected in more than 60% of the corresponding single cells and in a

small percentage of cells of other types (Table S3) and had a higher expression level than in other cells (according to a Wilcoxon rank sum test, and with logFC > 1.5).

Quantitative RT-PCR

RNA was extracted using the RNeasy Mini Kit (Qiagen). cDNA was then generated from 100 ng of RNA using the Superscript III Reverse Transcriptase Kit. Differential levels of cDNA expression were measured using droplet digital PCR (ddPCR)). Briefly, cDNA and primers were distributed into approximately 10000 to 20000 droplets. The nucleic acids were then PCR-amplified in a thermal cycler and read (as the number of positive and negative droplets) on a QX200 ddPCR system (Biorad, Hercules, CA, USA)). The ratio for each tested gene was normalized against the total number of positive droplets for *Gapdh* mRNA. The primer sequences are given in the key resource table. Three to five independent samples were analyzed in each experiment.

High-resolution fluorescent *in situ* hybridization

Fluorescent *in situ* hybridization (FISH) was performed on floating PBS/paraformaldehyde (PFA) 4% fixed brain sections or purified MVs immobilized on a glass slide coated with Cell-Tak (Corning) and fixed for 10 min in PBS/PFA 4%, according to the v2 Multiplex RNAscope technique (Advanced Cell Diagnostics, Inc., Newark, CA, USA) described previously (Oudart et al. 2020). Brain sections and MVs were treated with protease at room temperature. After the FISH, MVs were stained with isolectin B4 (1/100) in PBS/ normal goat serum (NGS) 5%/Triton 0.5% overnight at 4°C. Nuclei were stained with Hoechst reagent (1/2000). The brain sections and purified MVs were imaged using a Spinning Disk CSU-W1 microscope and Metamorph Premier 7.8 software.

FISH quantification

The mRNA density in vessels was analyzed using a newly developed "Vessel_Scope" ImageJ plugin (Rueden et al. 2017). In a calibration step, the intensity of a single mRNA dot was estimated in each experimental condition. Isolated dots were detected using the cell counter ImageJ plugin and segmented using the mcib3D library (Ollion et al. 2013). The background intensity was calculated for regions of interest drawn near each dot:

$$meandotInt.bg = \sum_{dotZmin}^{dotZmax} \frac{roiInteg.Intensity}{roiarea}$$

where dotZmin and dotZmax correspond to the dot's lower and upper z positions, respectively.

The background-corrected "single mRNA" intensity was then determined as:

$$\text{corrected "single mRNA" intensity} = \frac{\sum_{1}^{ndots}(\text{dotInteg.Int. - meandotInt.bg * dotVol})}{ndots}$$

Each 3D Z-stack image was then analyzed. MVs were segmented using 3D median filter and Li threshold. RNAScope dots were segmented using difference of Gaussian filter and Triangle threshold. Segmented objects were detected using the mcib3D library (Ollion et al. 2013). For each MV, the number of single mRNAs was defined as the total intensity of dots in the MV divided by the corrected "single mRNA" intensity. The mRNA density of each MV was calculated as the number of single mRNAs divided by the MV's volume. The MV diameters were measured using ImageJ.

Western blots

MV pellets were sonicated three times for 10 s at 20 Hz (Vibra cell VCX130) in 2% SDS and heated at 56°C in Laemmli loading buffer (Biorad). The protein content was measured using the Pierce 660 nm protein assay kit (Thermo Scientific, Waltham, MA, USA). 10 µg of proteins were separated by denaturing electrophoresis on a 4–15% Criterion™ TGX™ Precast Midi Protein Gel (Biorad) and then electrotransferred to nitrocellulose membranes using the Trans-blot Turbo Transfer System (Biorad). Membranes were hybridized, as described previously (Ezan et al. 2012). The antibodies used in the present study are listed in the key resource table. Horseradish peroxidase activity was visualized by enhanced chemiluminescence in a Western Lightning Plus system (Perkin Elmer, Waltham, MA, USA). Chemiluminescent imaging was performed on a *FUSION FX* system (Vilber, South Korea). The level of chemiluminescence for each antibody was normalized against the histone 3 staining on the membrane.

Clearing and immunohistochemical analysis of murine tissue samples

Mice were killed with pentobarbital (600 mg/kg, i.p.). Brains were removed and post-fixed in 4% PFA for 24 h at 4°C and then assessed using the "immunolabeling-enabled three-dimensional imaging of solvent-cleared organs" technique (Renier et al. 2014). The samples were first dehydrated with increasingly concentrated aqueous Methanol (MetOH) solutions (MetOH: 20%, 40%, 60%, 80%, and twice 100%, for 1 h each) at RT and then incubated in 66% dichloromethane (DCM, Sigma Aldrich)/33% MetOH overnight. After 2 washes in 100% MetOH, brains were incubated in 5% H_2O_2/MetOH overnight at RT, rehydrated with increasingly dilute aqueous MetOH solutions (80%, 60%, 40%, and 20%; 1h each). Before immunostaining, brains were permeabilized first for 2 x 1h at RT in 0.2% Triton X-100/PBS, for 24 h at 37°C in 0.16% Triton X-100/2.3% glycine/20% DMSO/PBS, and then for 2 days at 37°C in 0.16% Triton X-100/6% donkey serum/10% DMSO/PBS. Brains were incubated for 3 days at 37°C with primary antibody diluted in a 0.2 Tween/1% heparin/3% donkey serum/5% DMSO/PBS solution, washed 5 times during 24h at 37°C in 0.2% Tween20/1% heparin/PBS solution, incubated for 3 days at 37°C with secondary antibody diluted in a 0.2 Tween/1% heparin/3% donkey serum/PBS solution,

and another washed five times. The brain samples were then dehydrated again with a MetOH/H_2O series (20%, 40%, 60%, 80% and 100% for 1h each, and then 100% overnight) at RT. On the following day, brains were incubated for 3h in 66% DCM/33% MetOH and then twice for 15 min at RT in 100% DCM and lastly cleared overnight in dibenzyl ether. Cleared brains were imaged using a light sheet microscope and Inspector pro software (Lavision Biotec GmbH, Bielefeld, Germany) with a 3.2x, a light sheet NA of 0.156 and a step size of 3 µm for developmental analysis (P5 to P60); and with a 4x zoom, a light sheet NA of 0.144 and a step size of 3.5 µm for dorsal/lateral analysis. 3D reconstructions were visualized with Imaris software (Bitplane). For each cortical region of the somatosensory area (dorsal or lateral part), a volume of 1600 x 1700 x 550µm (xyz) starting 80 µm bellow the brain surface were analyzed using "surface" and "filament" tools in Imaris software (Oxford instruments, Oxford). The length and number of branch points of SMA-immunolabeled brain microvessels were quantified. Three brains were analyzed per developmental stage.

Immunohistochemical analysis of human tissue samples

The specimens described here are part of the "Hôpitaux Universitaires de l'Est Parisien – Neuropathologie du développement" brain collection (biobank identification number: BB-0033-00082). Informed consent was obtained for brain autopsy and histological examination. Fetal brains were obtained from spontaneous or medical abortions. The fetuses did not display any significant brain disorders or diseases. Analyzed samples: prenatal (15 week of gestation (wg); 21 wg; 28 wg; 30 wg; 39 wg); Postnatal (3 weeks; 1 month; 2 months; 3 months; 8 months; 1 year; 3 years; 4 years (n=2); 10 years; 11 years; 12 years; 13 years (n=2); 16 years; 17 years). One slice per sample was analyzed.

The same technical procedures were applied to all brain samples: after removal, brains were fixed with formalin for 5–12 weeks. A macroscopic analysis enabled the samples to be selected and processed (paraffin embedding, preparation of 7-micron slices, and staining with hematein reagent) for histological analysis. Coronal slices (including the temporal telencephalic parenchyma and the hippocampus) were deparaffinized and unmasked in citrate buffer (pH 6.0). Expression of MYH11 and SMA was detected using the Bond Polymer Refine Detection kit (Leica) and processed on automated immunostaining systems (the Bond RX Leica for MYH11, and the LEICA BOND III for SMA). Pictures were acquired using a slide scanner (Lamina, Perkin Elmer).

Stained samples were analyzed using the QuPath software (Bankhead et al. 2017). For each sample, a QuPath "pixel classifier" was trained to discriminate between DAB-positive spots and the background. This "classifier" consisted in an artificial neural network based on four features: a Gaussian filter to select for the intensity, and

three structure tensor eigenvalues to favor thin elongated objects. To train the classifier, we defined manually annotated spots and background area on one image per developmental stage. When the results were visually satisfactory, the trained pixel classifier was used to detect positive spots in manually defined regions of interest.

VSMC contractility *ex vivo*

Mice were rapidly decapitated, and the brains were quickly removed and placed in cold (~4°C) artificial cerebrospinal fluid (aCSF) solution containing 119 mM NaCl, 2.5 mM KCl, 2.5 mM $CaCl_2$, 26.2 mM $NaHCO_3$, 1 mM NaH_2PO_4, 1.3 mM $MgSO_4$, 11 mM D-glucose (pH = 7.35). Brains were constantly oxygenated with 95% O_2 –5% CO_2. Brain cortex slices (400 μm thick) were cut with a vibratome (VT2000S, Leica) and transferred to a constantly oxygenated (95% O_2–5% CO_2) holding chamber containing aCSF. Subsequently, individual slices were placed in a submerged recording chamber maintained at RT under an upright microscope (Zeiss) equipped with a CCD camera (Qimaging) and perfused at 2 mL/min with oxygenated aCSF. MVs at the junction between layers I and II of the somatosensory cortex and with a well-defined luminal diameter (10–15 μm) were selected. Only one MV per slice was analyzed. An image was acquired every 30 s. Each recording started with the establishment of a control baseline for 5 min. MVs with an unstable baseline (i.e. a change in diameter of more than 5%) were discarded from analysis. Vasoconstriction was induced by the application of the thromboxane A_2 receptor agonist U46619 (9,11-dideoxy-11a,9a- epoxymethanoprostaglandin F2α, 50 nM, Sigma) for 2 min. The signal was recorded until it had returned to the baseline.

Any drift in the images during the recording time was corrected either online (for z-drift) or off-line (for the x and y drift), using Image Pro Plus 7.0. To minimize the differences between two consecutive frames, images were manually repositioned using the subtraction tool in Image Pro Plus. Vasoconstriction was measured using a custom routine running in IgorPro (Wavemetrics).

Magnetic resonance imaging of the CBF

MRI was performed on a 7T Pharmascan MRI system (Bruker®, Germany) equipped with volume transmit and surface receive coils. To prevent motion on acquisition, the animals were anesthetized with isoflurane 2-3% in oxygen. The respiratory rate was regulated at 70-100 breaths per minute and temperature was maintained with a warming device. Total acquisition time did not exceed 20 minutes.

A fast T2 anatomical sequence was acquired before the arterial spin labeling (ASL) sequence to allow precise targeting of the slice of interest. Common anatomical features allowed the targeting of the wanted slice (bregma +1 mm) across our groups. The natively implemented ASL sequence on our Bruker MRI scanner was used with a 0.156 x 0.156 mm planar resolution in a single, 1 mm thick slice (matrix size: 128 x 128). Native ASL-calculating macros from Bruker where used for CBF estimations. CBF maps were computed from built-in Bruker macro. A 1 voxel (0.156 x 0.156 mm) gaussian filter was applied on the resulting map to smooth the voxel-wise calculations. CBF values were measured in right and left cortex and meaned for each subject before analysis. Measures on CBF maps were realized with FiJi (Schindelin et al. 2012).

Statistical tests

For most analysis a Kruskal-Wallis test was first performed to determine whether there is a global developmental effect, followed by a post-hoc Mann-Whitney comparison. A One-tailed Mann-Whitney test was used to test the null hypothesis "increased during development", based on the initial analysis of transcriptomic data. Exception are for (i) data presented in **Fig. 1B** for which a two-tailed Mann-Whitney was applied; (ii) FISH analysis (**Fig. 3E**) for which a Chi² test was first applied to analyse the difference in proportion between P5 and P15; (iii) The MRI study (**Fig. 5F, G**) for which data showed a normal distribution allowing to perform an ANOVA test followed by a Tukey's multiple hypothesis test to calculate p-values between developmental stages. Data are given in Table S4. In Fig. 5C. D, repeated measures from 3 different mice on each stage are presented. Kruskal-Wallis test was first performed to show absence of difference between animals of the same developmental stage (Maximum amplitude: P5, p=0.1; P15, p=0.8; P60, p=0.3) (Slope: P5, p=0.1; P15, p=0.9; P60, p=0.5).

Resources table

Reagent or resource	**Source**	**Reference**
Antibodies		
SMA (WB : 1/1000, IF : 1/250)	Sigma	C6198
MYH11 (IF / human slices: 1/50)	Sigma	HPA015310-100UL
Myh11 (Western Blot 1/1000)	Abcam	ab53219
Pecam-1 (IF: 1/300)	R&d systems	AF3628
Histone 3 (Western Blot: 1/2000)	Ozyme	14269S

anti-goat, alexa 647 (IF : 1/2000)	Thermo fisher	
anti-rabbit, HRP (WB : 1/2500)	Cohesion	CSA2115
anti-mouse, HRP (WB : 1/2500)	Cohesion	CSA2108
Alexa-conjugated Isolectin (*griffonia simplicifolia*)	Thermo fisher	I32450
FISH Probes		
Myh11	ACD/Biotechne	316101
qPCR Primers		
Tagln Forward CCCAGACACCGAAGCTACTC Reverse TCGATCCCTCAGGATACAGG	Sigma	
Acta2 Forward GTCCCAGACATCAGGGAGTAA Reverse TCGGATACTTCAGCGTCAGGA	Sigma	
Myh11 Forward AACGCCCTCAAGAGCAAACTCAGA Reverse TCCCGAGCGTCCATTTCTTCTTCA	Sigma	
Atp1b1 Forward GCTGCTAACCATCAGTGAACT Reverse GGGGTCATTAGGACGGAAGGA	Sigma	
Gapdh Forward AGGTCGGTGTGAACGGATTTG Reverse TGTAGACCATGTAGTTGAGGTCA	Sigma	
Tbxar2 Forward CCTTGTTCTCACCGACTTCC Reverse GCTGAACCATCATCTCCACC	Sigma	
qPCR probes		
Kcnj8	Thermofisher	Mm00438070_m1

Abcc9	Thermofisher	Mm00447761_m1
Pecam1	Thermofisher	Mm00487656_m1
Gapdh	Thermofisher	Mm00501337_m1
Software and Algorithms		
ImageJ	https://imagej.nih.gov/ij/	
QuPath	https://qupath.github.io/	
Deposited Data		
Raw data and analysis	This paper	GEO: GSE173844

Results

MVs follow a transcriptional maturation program between P5 and P15

Several studies in rodents have suggested that the brain's microvascular system architecture reorganizes after birth (Coelho-Santos et al. 2021; Coelho-Santos and Shih 2020). To characterize the molecular bases of these changes, we compared the transcriptome of brain mechanically-purified MVs (Boulay et al. 2015) on P5 and P15, two stages defining an important developmental window for the cerebrovascular system (Coelho-Santos et al. 2021; Coelho-Santos and Shih 2020) (**Fig. 1A**). We previously showed that purified MVs are composed by ECs, VSMC, PCs, FBs as well as perivascular astrocyte endfeet and neuronal fibers (Boulay et al. 2015). We limited our transcriptomic study to parenchymal MVs excluding large meningeal arteries and veins (see Materials and Methods) and focusing on the dorsal part of the cortex since vascular properties and developmental programs differ from one region of the brain to another. Prior to this analysis, we assessed by qPCR the expression level of known endothelial and pericyte specific transcripts and compared the pericyte/endothelial ratio in mechanically purified cortical MVs and whole cortex on P5 and P15 (**Fig. 1B**). They were identical at both stages indicating that mechanical purification preserved the cellular composition of MVs and is a powerful tool for the molecular characterization of brain vascular cells (**Fig. 1B**). mRNAs extracted from cortical MVs were sequenced. Heat map analysis showed a clear clustering between P5 and P15 libraries (**Fig. 1C**). 11286 transcripts with more than 50 reads in at least one stage were identified (**Fig. 1D; Table S1**). 10355 of the transcripts (92 %) were equally expressed at both time points ($-1 < \log2$ fold-change (FC) < 1 or adjusted p-value (padj) > 0.05), and only 931 (8 %) differed significantly between P5 and P15 ($\log2FC \leq -1$ or $\log2FC \geq 1$ and $padj \leq 0.05$). 484 of these 931 (52 %) transcripts were upregulated on P15 ($\log2FC \geq 1$ and $padj \leq 0.05$), and 447 (48 %) were downregulated ($\log2FC \leq -1$ and $padj \leq 0.05$) (**Fig. 1D**). These results indicated that transcription in vascular cells is mostly stable but differs significantly in some respects between P5 and P15. To further characterize these differences, we performed a gene ontology (GO) of the biological processes (**Fig. 1E; Table S2),** KEGG and REACTOME pathway analyses of our RNA sequencing (RNAseq) data (**Table S2**). Transcripts downregulated on P15 mostly related to cell cycle (DNA replication, cell division), while pathways related to ECM composition, cell adhesion and ion transport were upregulated **(Fig. 1E)**. These results suggested a possible molecular switch of MV cells from angiogenesis to the acquisition of specific functions.

Hence, cortical MVs are mostly stable but follow a transcriptional maturation program between P5 and P15.

Characterization of postnatal transcriptional maturation in brain microvessel cells

We next sought to characterize the maturation of each vascular cell type of MVs. By taking advantage of recently published single cell RNASeq datasets for adult brain vascular cells, we started by identifying the genes preferentially or specifically expressed in ECs, PCs, VSMCs and FBs (He et al. 2016; Vanlandewijck et al. 2018) and we determined their expression level in MVs on P5 and P15 (**Fig. 2A**). A transcript was considered to be preferentially expressed in a cell type when it was (i) detected in more than 60% of the single cells of that type and in a small percentage of other cells and (ii) expressed at a higher level than in other cells (LogFC ≥ 1.5). This approach led to the identification of 73 EC-, 14 PC-, 38 FB- and 21 VSMC- transcripts (**Table S3**). We then analyzed the FC for each transcript in MVs between P5 and P15: 11, 12 and 10 transcripts were (log2FC ≥ 1 and padj ≤ 0.05) upregulated on P15 in ECs, FBs and VSMCs, respectively, and 1 and 1 transcripts were downregulated (log2FC ≤ -1 and padj ≤ 0.05) on P15 in FBs and VSMCs, respectively (**Fig. 2B; Table S3**).

We next focused on VSMC's molecular maturation between P5 and P15. Interestingly, all VSMC-specific or -preferentially expressed transcripts upregulated on P15 encoded proteins contributing to contractility, such as *Acta2* (coding for SMA), *Tpm2* (tropomyosin2), *Myh11* (myosin heavy chain 11) and *Tagln* (SM22/transgelin) (**Fig. 2C**). RNAseq results were validated on a selection of genes using qPCRs on MVs purified from whole brain (**Fig. 3A).** As a control, we included in this analysis *Atp1b1*, a VSMC-specific transcript whose expression was unchanged between P5 and P15 (**Table S3**). We then performed a fluorescent *in situ* hybridization (FISH) analysis of *Myh11* (encoding myosin heavy chain 11) on cortical slices **(Fig. 3B**). On P5, few *Myh11* FISH dots were found in the vessels or the parenchyma. In contrast, large vessels gave an intense signal on P15 **(Fig. 3B**). To quantify these differences, we next performed FISH on whole-brain purified MVs **(Fig. 3C)**. A first quantification of the analyzed vessel diameter indicated a higher diameter on P15 (**Fig. 3D**). On P5, *Myh11* FISH dots were detected in most MVs at a moderate density (10-100 x 10^{-3} dots.µm^{-3}) (**Fig. 3C, E; Table S4**). On P15, the proportion of unlabeled (0-10 x 10^{-3}dots.µm^{-3}) small-diameter vessels (mean: 5.9 µm ± 3.0) was higher, as was the proportion of densely labeled (>100 x 10^{-3} dots.µm^{-3}) larger-diameter (mean: 13.5 µm ± 5.6) vessels (**Fig. 3C, E, F; Table S4**). These data highlighted a change in *Myh11* expression from low and diffuse on P5 to high and large vessel-specific on P15.

Considering our data as a whole, we identified a set of specific or preferentially-expressed transcripts for each brain vascular cell type and characterized their expression within MVs between P5 and P15. These findings

suggest that these brain vascular cells undergo a transcriptional maturation between P5 and P15. Focusing on VSMCs, our results show that this transcriptional maturation relates to contractile properties.

VSMCs acquire contractile properties during postnatal development in mice with heterogenous developmental trajectories within cortical regions.

Our data indicated that the transcription of VSMC-specific genes encoding contractile proteins was upregulated between P5 and P15. To further study this progression, we used Western blotting to analyze the protein levels of SMA and Myh11 in protein extracts from MVs purified from whole brain on P5, P15, P30 and P60. Levels of both proteins rose progressively (**Fig. 4A**). To further characterize the postnatal maturation of VSMCs, we next used an immunofluorescence assay to analyze the SMA-positive vascular network in the dorsal part of the somatosensory cortex on cleared brain samples from P5, P15 and P60 (**Fig. 4B, C**). The endothelial network was counterstained with an anti-Pecam-1 antibody (**Fig. 5C**). In the parenchyma of this cortical region, we observed that the SMA-positive vascular network became progressively denser. Interestingly, the number of SMA-positive primary branches (penetrating arterioles) did not change significantly over time (**Fig. 4B-D**). However, the total number of SMA-positive branches and ramifications rose progressively (**Fig. 4B-D)**.

To address the functional consequences of these changes, we first compared the *ex vivo* myogenic tone of VSMCs on brain slices sampled on P5, P15 and P60. Of note the absence of perfusion and intraluminal pressure in brain slices result in vessels being maximally dilated (Iadecola and Nedergaard 2007). Thus we focused on VSMC contractility and recorded the change in lumen diameter of cortical arterioles upon exposure for 2 min to a thromboxane A_2 receptor agonist U46619 (9,11-dideoxy-11a,9a-epoxymethanoprostaglandin F2α), which is known to induce reversible vasoconstriction (Perrenoud et al. 2012) (**Fig. 5A-C**). As previously observed (**Fig. 3D**), mean diameter of cortical arterioles measured before U46619 exposure was higher on P15 compared to P5 and identical between P15 and P60 (**Fig. 5D**). It should be noted that according to our RNAseq data, the level of transcription of *Tbxa2r* (encoding the thromboxane A_2 receptor) did not change between P5 and P15 (log2FC = -0.3, padj = 0.5) (**Table S1**). This finding was confirmed by qPCR on MVs purified from whole brain (**Fig. 5E**). The amplitude of vasoconstriction was assessed as the percentage reduction in vessel diameter upon application of U46619. The slope indicated the velocity of this vasoconstriction. On P5, application of U46619 had a small effect on vessel diameter (**Fig. 5A-C**). In contrast, the amplitude of vasoconstriction was significantly higher on P15 and even higher again on P60 - indicating that VSMC contractility continues to progress after P15. Thus, in the mouse cortex, arteriolar contractility rose progressively after birth.

Since VSMC contractility promotes the CBF (Nippert et al. 2018), we next measured the cortical CBF on P5 and P15 by arterial spin labeling (ASL) magnetic resonance imaging (MRI) **(Fig. 5F, G)** (Detre et al. 2012). On P5, CBF was significantly lower than P15 and P30, while it did not significantly differ between P15 and P30 mice (**Fig. 5F, G)**. Interestingly, the ratio between the dorsal and lateral parts of the cortex was higher at P30 compared to P15 indicating that CBF in the cortex is not homogenous at P15 and continues its maturation between P15 and P30 in the dorsal part of the cortex (**Fig. 5F, G**). To determine if this heterogeneity could relate to the acquisition of VSMCs contractility, we analyzed the SMA-immunolabeled cortical vascular network on cleared brain samples as previously (**Fig. 4B-D**) focusing on dorsal and lateral areas of the somatosensory cortex on P15. A denser and more ramified SMA-positive vascular network was observed in the lateral part of the cortex (**Fig. 5H, I**). In addition, on P15, SMA level analyzed by Western blotting was higher in MVs purified from the lateral part of the cortex compared to dorsal part (**Fig. 5J**).

Overall, these results demonstrate that the VSMC network expands and complexifies after birth with heterogenous developmental trajectories within cortical regions and that VSMCs progressively acquire postnatally their molecular and functional contractile properties contributing to the maturation of the CBF.

The VSMC contractile network matures postnatally in the human cortex

We finally looked at whether the vascular network in humans also matured after birth by measuring MYH11 and SMA expression on human cortical slices from 15 weeks of gestation (wg) to 17 years of age using an immunohistochemical assay (**Fig. 6**). In prenatal samples (from 15 to 39 wg), a MYH11 signal was detected in the meninges but not in the parenchyma (**Fig. 6Ai**). In contrast, penetrating arteries were intensely labeled after birth (**Fig. 6Aii**). After 2 years of age, a large number of MYH11-immunolabeled vessels were observed throughout the parenchyma (**Fig. 6Aiii and iv**). Hence, we quantified a progressive increase in MYH11-positive surface area and the number of MYH11-positive vessels from birth to the age of 2 to 5 years (**Fig. 6B**). In contrast to MYH11, SMA was already detected in few penetrating arterioles at prenatal stages (**Fig. 6Ci**) and a progressive increase of SMA-positive surface area and the number of SMA-positive vessels was observed from birth to the age of 2 to 5 years (**Fig. 6Cii and iii, D**).

In conclusion, these results testify to expansion and complexification of the arteriolar VSMC cortical network after birth in the human.

Discussion

The development of the brain's microvascular system during embryogenesis has been well described. In contrast, data on the microvascular system's molecular and functional postnatal maturation are scarce. Here, we demonstrated that vascular cells in the mouse and the human follow postnatal transcriptional programs. In particular, we highlighted the postnatal acquisition of contractility by arteriolar VSMCs both in mice and human.

Our analysis of the postnatal maturation of brain vascular cells was firstly based on the transcriptional analysis of parenchymal MVs mechanically purified from the mouse cortex on P5 and P15. This technique has several advantages. Firstly, the vascular cells were not exposed to enzyme treatments that might induce transcriptomic changes. Secondly, this MV preparation enabled us to probe the contribution of all the component cell types while maintaining the *in vivo* ratio between the latter. Our comparison of P5 and P15 MVs revealed that the transcriptome was stable overall: changes were observed for only 8% of the genes. Nevertheless, our pathway analysis highlighted the upregulation of genes specifically related to ECM composition, cell junctions and ion transport and thus evidence the functional maturation of MVs between P5 and P15. In contrast, we observed the downregulation of pathways related to DNA replication, cell division and the cell cycle, suggesting that the putative angiogenic program involved in the postnatal densification of the capillary network was less active on P15.

We next focused on transcripts that were preferentially expressed in each vascular cell type. We identified these transcripts by checking brain vessel single-cell RNAseq databases (He et al. 2016; Vanlandewijck et al. 2018). Our analysis therefore focused on the transcriptional signature of each vascular cell type, rather than overlaps in molecular repertoires between cell types. Of note, the single-cell RNAseq database used as a reference in our study has been generated from mice aged 10-19 weeks (adult stage) and we assumed here that the cellular identity of preselected transcripts is stable during development, which might not be the case for all genes. Several transcripts encoding ECM components were specifically expressed by FBs, confirming that these cells actively contribute to the BL (Manberg et al. 2021) and (possibly) its postnatal development because some genes (*Ctgf, Serping1, Lum, Col6a1, Col5a1* and *Lama1*) were more strongly expressed on P15 than on P5. The recruitment of perivascular FBs and their differentiation has not previously been fully described. The literature data suggest that perivascular FBs are recruited from the meninges after birth (Kelly et al. 2016);(Bonney et al. 2022; Dorrier et al. 2022). Here, we found that half of the FB transcripts were upregulated between P5 and P15; hence, postnatal molecular maturation might also cover the FBs. Our list of PC-preferentially expressed transcripts was consistent with previous transcriptomic analyses (Chasseigneaux et al. 2018; Bondjers et al. 2006); in particular, we identified

Kcnj8 (encoding the ATP-sensitive inward rectifier potassium channel Kir6.1) and *Abcc9* (encoding the ABC transporter 9) involved in ion transport and intercellular signaling (Nelson et al. 2015). Of note, these transcripts have recently been found in brain MC progenitors and would sustain brain VSMC differentiation (Ando et al. 2022). Interestingly, expression of all the PC-preferentially expressed transcripts did not differ significantly when comparing P5 and P15; this suggests that PC differentiation and maturation are already complete on P5. Our P5-P15 comparison of MVs showed that some EC-specific or -preferentially expressed transcripts were upregulated, thus indicating that ECs continued to mature after birth. The expression levels of transcripts of TJ proteins or TJ-associated proteins were similar on P5 and P15 cortical MVs. These results are in line with previous reports in which the barrier function was fully established during embryogenesis (by around E15) in the mouse (Daneman et al. 2010). In contrast, expression of some ABC and SLC transport proteins which control molecular access to the brain parenchyma such as *Abcb1a* (coding for P-gP) or *Slco1a4* (Oatp1a4)showed levels increased from P15 to P30 in mouse MVs indicating that the brain accessibility to drug follows a postnatal maturation in the mouse.

The vast majority of VSMC-preferentially expressed or -specific transcripts identified in our study were related to muscle differentiation and contractility. Apart from well-known VSMCs transcripts (such as *Acta2*, *Myh11*, *desmin* and *Tgln*), our analysis highlighted the expression of markers like *NR4a1* (coding for nuclear receptor subfamily 4, group A, member 1, involved in SMC proliferation) (Yu et al. 2015), *Pdlim3* (coding for actinin-associated LIM protein), involved in myocyte stability (Zheng et al. 2010), *Mustn1* (regulating myoblast differentiation) (Hadjiargyrou 2018), and *Pln* (coding for phospholamban), which regulates the sarcoplasmic reticulum Ca^{2+}ATPase (SERCA) activity and muscle contractility (Kranias and Hajjar 2012). Surprisingly, about half of the genes were strongly upregulated on P15; this indicates that arteriolar VSMC contractility continued to differentiate between P5 and P15. It is noteworthy that some of these transcripts were expressed (albeit at a much lower level) by PCs. Our FISH analysis showed that the strongest expression of *Myh11* on P15 was limited to the largest MVs, thus expressed by arteriolar VSMCs. However, we cannot exclude the contribution of few PCs expressing contractile proteins, in particular at the level of pre-capillary arterioles (Hartmann et al. 2021).

We revealed an increased expression of contractile proteins in arteriolar VSMCs from P5 in the mouse. Parenchymal MYH11 immunoreactivity appearance in the first two years after birth in the human cortex indicated that the same molecular maturation also occurs in humans. Furthermore, we observed a progressive increase in the number of SMA-positive vessels in the mouse (from P5 to P60) and SMA and MYH11-positive vessels in humans (up until the age of two), which shows that the arteriolar network continues its densification postnatally. Our *ex vivo* and *in vivo* observations of the progressive acquisition of cortical arteriole contractility and the marked CBF

increase between P5 and P15 indicated that arteriolar VSMCs molecular maturation results in a postnatal phenotypic contractile switch contributing to the brain perfusion. Taken as a whole, our results in the mouse and the human strongly suggest that the myogenic tone of parenchymal arterioles, which determines vascular tone and brain perfusion, is acquired progressively after birth.

It is thought that during embryogenesis, VSMCs are recruited to newly formed vessels in two ways: (i) the *de novo* formation of VSMCs via the induction of undifferentiated perivascular mesenchymal cells, and (ii) the migration of VSMCs from a preexisting pool (Hellstrom et al. 1999). VSMC differentiation is regulated by several signaling pathways (including VEGFA, Notch, EphrinB2/B4, PDGFß and TGFß pathways). It would be interesting to address these pathways' role during the postnatal period. The same mechanisms might operate during the VSMC network's postnatal expansion, along with the recently described K-ATP-dependent mechanisms in postnatal VSMC differentiation (Ando et al. 2022).

Microvessel contractility is crucial to the neurovascular coupling, i.e the capacity of the vascular system to locally adapt blood flow to neuronal activity. Here we observed an increase in CBF in postnatal mice. Of note, experiments were performed under isoflurane anesthesia, a known vasodilator (Sullender et al. 2022), which might modify the CBF. Interestingly, CBF on P15 showed a dorso-lateral cortical heterogeneity, which we could correlate with the level of SMA and the density of the SMA^+ arteriolar network. These data therefore strongly support the idea that the postnatal acquisition of arteriolar VSMC contractility is a mandatory element in the CBF maturation process. Other recent studies suggested that the neurovascular coupling in neonates and preterm born infants differs compared to adults (Anderson et al. 2001; Kusaka et al. 2004), although adult-like cerebral haemodynamic responses were also reported in infants born preterm (Arichi et al. 2010) and 2-4 month-old infants (Taga et al. 2003). In rodents, a progression of the hemodynamic response was described from P7 to the adult (Colonnese et al. 2008; Kozberg et al. 2013; Zehendner et al. 2013) and has been attributed to the immaturity of most of the cellular components involved in the hemodynamic response, i.e. astrocytic and synaptic connectivity, vascular network and myelination are still in development at birth. Our study now indicates that the postnatal acquisition of arteriolar VSMC contractility is likely to be another element in this maturation process.

From a medical and pharmacological point of view, our results are crucial. Indeed, non-invasive MRI studies of intracranial aneurysms have shown that cortical blood flow was altered in preterm (before 36 wg) compared to term newborns (Chalouhi et al. 2012). The maturation of the brain vasculature's responsiveness is associated with differential responses to vasoactive drugs in preterm, term newborns, and adults. The best vasoactive drugs for the management of neonatal systemic hypotension might not be those used for the same

purpose in adults (Toth-Heyn and Cataldi 2012). Lastly, impairments of arteriolar VSMC differentiation and contractility have been linked to several small-vessel diseases, such as cerebral aneurysm (Chalouhi et al. 2012), arteriovenous malformations, and cerebral cavernous malformations (Uranishi et al. 2001; Frosen and Joutel 2018). In view of our results, impairments in the arteriolar VSMCs' postnatal differentiation might also be involved in these diseases.

In conclusion, our present results revealed that the parenchymal cerebral microvasculature in the mouse and in the human undergoes a profound molecular maturation after birth. This maturation results in particular in the acquisition of VSMC contractility which governs cerebral perfusion and neurovascular coupling; hence, this maturation is a crucial step in the acquisition of brain functions and might guide treatment approaches in pediatric medicine.

Acknowledgments

This work was funded by grants from the *Association Européenne contre les Leucodystrophies* (ELA) (ELA2012-014C2B), the *Fondation pour la Recherche Médicale* (FRM) (AJE20171039094) and the *Fondation Maladies Rares* (20170603). A. Gilbert's PhD fellowship was funded by the FRM (PLP20170939025p60) and ELA (ELA2012-014C2B). L. Slaoui's fellowship PhD was funded by the Ecole Normale Supérieure. A.-C. Boulay's work was funded by the FRM (AJE20171039094) and the *Foundation pour la recherche sur la sclérose en plaques* (ARSEP). Despite our efforts, our work has not received any support from the French National Agency for Research (ANR).

Author contributions

Conceptualization, M.C-S. and A-C.B.; Methodology, M.C-S., A-C.B., P.M., G.L., A.G., N.R., D.V., A.R.; Investigation, L.S., A.G., B.D-P, M.B.L, L.F., S. C., A.R., A.C., Q.G., M.F., K.D., L.J., S.A., A-C.B., M. C-S; Writing – Original Draft, M.C-S.; Funding Acquisition, M.C-S.; Supervision, M.C-S. and A-C.B.

The authors declare no competing financial interests

This article contains 4 supplementary Tables

References

Anderson AW, Marois R, Colson ER, Peterson BS, Duncan CC, Ehrenkranz RA, Schneider KC, Gore JC, Ment LR (2001) Neonatal auditory activation detected by functional magnetic resonance imaging. Magn Reson Imaging 19 (1):1-5. doi:10.1016/s0730-725x(00)00231-9

Ando K, Tong L, Peng D, Vazquez-Liebanas E, Chiyoda H, He L, Liu J, Kawakami K, Mochizuki N, Fukuhara S, Grutzendler J, Betsholtz C (2022) KCNJ8/ABCC9-containing K-ATP channel modulates brain vascular smooth muscle development and neurovascular coupling. Dev Cell 57 (11):1383-1399 e1387. doi:10.1016/j.devcel.2022.04.019

Arichi T, Moraux A, Melendez A, Doria V, Groppo M, Merchant N, Combs S, Burdet E, Larkman DJ, Counsell SJ, Beckmann CF, Edwards AD (2010) Somatosensory cortical activation identified by functional MRI in preterm and term infants. Neuroimage 49 (3):2063-2071. doi:10.1016/j.neuroimage.2009.10.038

Attwell D, Mishra A, Hall CN, O'Farrell FM, Dalkara T (2016) What is a pericyte? J Cereb Blood Flow Metab 36 (2):451-455. doi:10.1177/0271678X15610340

Bankhead P, Loughrey MB, Fernandez JA, Dombrowski Y, McArt DG, Dunne PD, McQuaid S, Gray RT, Murray LJ, Coleman HG, James JA, Salto-Tellez M, Hamilton PW (2017) QuPath: Open source software for digital pathology image analysis. Sci Rep 7 (1):16878. doi:10.1038/s41598-017-17204-5

Ben-Zvi A, Liebner S (2021) Developmental regulation of barrier- and non-barrier blood vessels in the CNS. J Intern Med. doi:10.1111/joim.13263

Bondjers C, He L, Takemoto M, Norlin J, Asker N, Hellstrom M, Lindahl P, Betsholtz C (2006) Microarray analysis of blood microvessels from PDGF-B and PDGF-Rbeta mutant mice identifies novel markers for brain pericytes. FASEB J 20 (10):1703-1705. doi:fj.05-4944fje [pii]

10.1096/fj.05-4944fje

Bonney SK, Sullivan LT, Cherry TJ, Daneman R, Shih AY (2022) Distinct features of brain perivascular fibroblasts and mural cells revealed by in vivo two-photon imaging. J Cereb Blood Flow Metab 42 (6):966-978. doi:10.1177/0271678X211068528

Boulay AC, Saubamea B, Decleves X, Cohen-Salmon M (2015) Purification of Mouse Brain Vessels. J Vis Exp 105 (105). doi:10.3791/53208

Butler A, Hoffman P, Smibert P, Papalexi E, Satija R (2018) Integrating single-cell transcriptomic data across different conditions, technologies, and species. Nat Biotechnol 36 (5):411-420. doi:10.1038/nbt.4096

Chalouhi N, Ali MS, Jabbour PM, Tjoumakaris SI, Gonzalez LF, Rosenwasser RH, Koch WJ, Dumont AS (2012) Biology of intracranial aneurysms: role of inflammation. J Cereb Blood Flow Metab 32 (9):1659-1676. doi:10.1038/jcbfm.2012.84

Chasseigneaux S, Moraca Y, Cochois-Guegan V, Boulay AC, Gilbert A, Le Crom S, Blugeon C, Firmo C, Cisternino S, Laplanche JL, Curis E, Decleves X, Saubamea B (2018) Isolation and differential transcriptome of vascular smooth muscle cells and mid-capillary pericytes from the rat brain. Sci Rep 8 (1):12272. doi:10.1038/s41598-018-30739-5

Coelho-Santos V, Berthiaume AA, Ornelas S, Stuhlmann H, Shih AY (2021) Imaging the construction of capillary networks in the neonatal mouse brain. Proc Natl Acad Sci U S A 118 (26). doi:10.1073/pnas.2100866118

Coelho-Santos V, Shih AY (2020) Postnatal development of cerebrovascular structure and the neurogliovascular unit. Wiley Interdiscip Rev Dev Biol 9 (2):e363. doi:10.1002/wdev.363

Colonnese MT, Phillips MA, Constantine-Paton M, Kaila K, Jasanoff A (2008) Development of hemodynamic responses and functional connectivity in rat somatosensory cortex. Nat Neurosci 11 (1):72-79. doi:10.1038/nn2017

Daneman R, Zhou L, Kebede AA, Barres BA (2010) Pericytes are required for blood-brain barrier integrity during embryogenesis. Nature 468 (7323):562-566. doi:nature09513 [pii]

10.1038/nature09513

Detre JA, Rao H, Wang DJ, Chen YF, Wang Z (2012) Applications of arterial spin labeled MRI in the brain. J Magn Reson Imaging 35 (5):1026-1037. doi:10.1002/jmri.23581

Dobin A, Davis CA, Schlesinger F, Drenkow J, Zaleski C, Jha S, Batut P, Chaisson M, Gingeras TR (2013) STAR: ultrafast universal RNA-seq aligner. Bioinformatics 29 (1):15-21. doi:10.1093/bioinformatics/bts635

Dore-Duffy P (2008) Pericytes: pluripotent cells of the blood brain barrier. Curr Pharm Des 14 (16):1581-1593

Dorrier CE, Jones HE, Pintaric L, Siegenthaler JA, Daneman R (2022) Emerging roles for CNS fibroblasts in health, injury and disease. Nat Rev Neurosci 23 (1):23-34. doi:10.1038/s41583-021-00525-w

Ezan P, Andre P, Cisternino S, Saubamea B, Boulay AC, Doutremer S, Thomas MA, Quenech'du N, Giaume C, Cohen-Salmon M (2012) Deletion of astroglial connexins weakens the blood-brain barrier. J Cereb Blood Flow Metab 32 (8):1457-1467. doi:jcbfm201245 [pii]

10.1038/jcbfm.2012.45

Frosen J, Joutel A (2018) Smooth muscle cells of intracranial vessels: from development to disease. Cardiovasc Res 114 (4):501-512. doi:10.1093/cvr/cvy002

Hadjiargyrou M (2018) Mustn1: A Developmentally Regulated Pan-Musculoskeletal Cell Marker and Regulatory Gene. Int J Mol Sci 19 (1). doi:10.3390/ijms19010206

Hall CN, Reynell C, Gesslein B, Hamilton NB, Mishra A, Sutherland BA, O'Farrell FM, Buchan AM, Lauritzen M, Attwell D (2014) Capillary pericytes regulate cerebral blood flow in health and disease. Nature 508 (7494):55-60. doi:nature13165 [pii]

10.1038/nature13165

Hartmann DA, Berthiaume AA, Grant RI, Harrill SA, Koski T, Tieu T, McDowell KP, Faino AV, Kelly AL, Shih AY (2021) Brain capillary pericytes exert a substantial but slow influence on blood flow. Nat Neurosci 24 (5):633-645. doi:10.1038/s41593-020-00793-2

Hartmann DA, Underly RG, Grant RI, Watson AN, Lindner V, Shih AY (2015) Pericyte structure and distribution in the cerebral cortex revealed by high-resolution imaging of transgenic mice. Neurophotonics 2 (4):041402. doi:10.1117/1.NPh.2.4.041402

15009SSR [pii]

He L, Vanlandewijck M, Raschperger E, Andaloussi Mae M, Jung B, Lebouvier T, Ando K, Hofmann J, Keller A, Betsholtz C (2016) Analysis of the brain mural cell transcriptome. Sci Rep 6:35108. doi:srep35108 [pii]

10.1038/srep35108

Hellstrom M, Kalen M, Lindahl P, Abramsson A, Betsholtz C (1999) Role of PDGF-B and PDGFR-beta in recruitment of vascular smooth muscle cells and pericytes during embryonic blood vessel formation in the mouse. Development 126 (14):3047-3055

Huang da W, Sherman BT, Lempicki RA (2009) Systematic and integrative analysis of large gene lists using DAVID bioinformatics resources. Nat Protoc 4 (1):44-57. doi:10.1038/nprot.2008.211

Huang DW, Sherman BT, Tan Q, Kir J, Liu D, Bryant D, Guo Y, Stephens R, Baseler MW, Lane HC, Lempicki RA (2007) DAVID Bioinformatics Resources: expanded annotation database and novel algorithms to better extract biology from large gene lists. Nucleic Acids Res 35 (Web Server issue):W169-175. doi:10.1093/nar/gkm415

Iadecola C, Nedergaard M (2007) Glial regulation of the cerebral microvasculature. Nat Neurosci 10 (11):1369-1376. doi:10.1038/nn2003

Kelly KK, MacPherson AM, Grewal H, Strnad F, Jones JW, Yu J, Pierzchalski K, Kane MA, Herson PS, Siegenthaler JA (2016) Col1a1+ perivascular cells in the brain are a source of retinoic acid following stroke. BMC Neurosci 17 (1):49. doi:10.1186/s12868-016-0284-5

Kozberg MG, Chen BR, DeLeo SE, Bouchard MB, Hillman EM (2013) Resolving the transition from negative to positive blood oxygen level-dependent responses in the developing brain. Proc Natl Acad Sci U S A 110 (11):4380-4385. doi:10.1073/pnas.1212785110

Kranias EG, Hajjar RJ (2012) Modulation of cardiac contractility by the phospholamban/SERCA2a regulatome. Circ Res 110 (12):1646-1660. doi:10.1161/CIRCRESAHA.111.259754

Kusaka T, Kawada K, Okubo K, Nagano K, Namba M, Okada H, Imai T, Isobe K, Itoh S (2004) Noninvasive optical imaging in the visual cortex in young infants. Hum Brain Mapp 22 (2):122-132. doi:10.1002/hbm.20020

Lendahl U, Nilsson P, Betsholtz C (2019) Emerging links between cerebrovascular and neurodegenerative diseases-a special role for pericytes. EMBO Rep 20 (11):e48070. doi:10.15252/embr.201948070

Manberg A, Skene N, Sanders F, Trusohamn M, Remnestal J, Szczepinska A, Aksoylu IS, Lonnerberg P, Ebarasi L, Wouters S, Lehmann M, Olofsson J, von Gohren Antequera I, Domaniku A, De Schaepdryver M, De Vocht J, Poesen K, Uhlen M, Anink J, Mijnsbergen C, Vergunst-Bosch H, Hubers A, Klappe U, Rodriguez-Vieitez E, Gilthorpe JD, Hedlund E, Harris RA, Aronica E, Van Damme P, Ludolph A, Veldink J, Ingre C, Nilsson P, Lewandowski SA (2021) Altered perivascular fibroblast activity precedes ALS disease onset. Nat Med 27 (4):640-646. doi:10.1038/s41591-021-01295-9

Nakagomi T, Nakano-Doi A, Kawamura M, Matsuyama T (2015) Do Vascular Pericytes Contribute to Neurovasculogenesis in the Central Nervous System as Multipotent Vascular Stem Cells? Stem Cells Dev 24 (15):1730-1739. doi:10.1089/scd.2015.0039

Nelson PT, Jicha GA, Wang WX, Ighodaro E, Artiushin S, Nichols CG, Fardo DW (2015) ABCC9/SUR2 in the brain: Implications for hippocampal sclerosis of aging and a potential therapeutic target. Ageing Res Rev 24 (Pt B):111-125. doi:10.1016/j.arr.2015.07.007

Nippert AR, Biesecker KR, Newman EA (2018) Mechanisms Mediating Functional Hyperemia in the Brain. Neuroscientist 24 (1):73-83. doi:10.1177/1073858417703033

Noli L, Capalbo A, Ogilvie C, Khalaf Y, Ilic D (2015) Discordant Growth of Monozygotic Twins Starts at the Blastocyst Stage: A Case Study. Stem Cell Reports 5 (6):946-953. doi:10.1016/j.stemcr.2015.10.006

Ollion J, Cochennec J, Loll F, Escude C, Boudier T (2013) TANGO: a generic tool for high-throughput 3D image analysis for studying nuclear organization. Bioinformatics 29 (14):1840-1841. doi:10.1093/bioinformatics/btt276

Oudart M, Tortuyaux R, Mailly P, Mazare N, Boulay AC, Cohen-Salmon M (2020) AstroDot - a new method for studying the spatial distribution of mRNA in astrocytes. J Cell Sci 133 (7). doi:10.1242/jcs.239756

Perrenoud Q, Rossier J, Ferezou I, Geoffroy H, Gallopin T, Vitalis T, Rancillac A (2012) Activation of cortical 5-HT(3) receptor-expressing interneurons induces NO mediated vasodilatations and NPY mediated vasoconstrictions. Front Neural Circuits 6:50. doi:10.3389/fncir.2012.00050

Renier N, Wu Z, Simon DJ, Yang J, Ariel P, Tessier-Lavigne M (2014) iDISCO: a simple, rapid method to immunolabel large tissue samples for volume imaging. Cell 159 (4):896-910. doi:10.1016/j.cell.2014.10.010

Rueden CT, Schindelin J, Hiner MC, DeZonia BE, Walter AE, Arena ET, Eliceiri KW (2017) ImageJ2: ImageJ for the next generation of scientific image data. BMC Bioinformatics 18 (1):529. doi:10.1186/s12859-017-1934-z

Rungta RL, Chaigneau E, Osmanski BF, Charpak S (2018) Vascular Compartmentalization of Functional Hyperemia from the Synapse to the Pia. Neuron 99 (2):362-375 e364. doi:10.1016/j.neuron.2018.06.012

Saunders A, Macosko EZ, Wysoker A, Goldman M, Krienen FM, de Rivera H, Bien E, Baum M, Bortolin L, Wang S, Goeva A, Nemesh J, Kamitaki N, Brumbaugh S, Kulp D, McCarroll SA (2018) Molecular Diversity and Specializations among the Cells of the Adult Mouse Brain. Cell 174 (4):1015-1030 e1016. doi:10.1016/j.cell.2018.07.028

Schindelin J, Arganda-Carreras I, Frise E, Kaynig V, Longair M, Pietzsch T, Preibisch S, Rueden C, Saalfeld S, Schmid B, Tinevez JY, White DJ, Hartenstein V, Eliceiri K, Tomancak P, Cardona A (2012) Fiji: an open-source platform for biological-image analysis. Nat Methods 9 (7):676-682. doi:10.1038/nmeth.2019

Sullender CT, Richards LM, He F, Luan L, Dunn AK (2022) Dynamics of isoflurane-induced vasodilation and blood flow of cerebral vasculature revealed by multi-exposure speckle imaging. J Neurosci Methods 366:109434. doi:10.1016/j.jneumeth.2021.109434

Supek F, Bosnjak M, Skunca N, Smuc T (2011) REVIGO summarizes and visualizes long lists of gene ontology terms. PLoS One 6 (7):e21800. doi:10.1371/journal.pone.0021800

Taga G, Asakawa K, Maki A, Konishi Y, Koizumi H (2003) Brain imaging in awake infants by near-infrared optical topography. Proc Natl Acad Sci U S A 100 (19):10722-10727. doi:10.1073/pnas.1932552100

Toth-Heyn P, Cataldi L (2012) Vasoactive compounds in the neonatal period. Curr Med Chem 19 (27):4633-4639. doi:10.2174/092986712803306330

Uranishi R, Baev NI, Kim JH, Awad IA (2001) Vascular smooth muscle cell differentiation in human cerebral vascular malformations. Neurosurgery 49 (3):671-679; discussion 679-680. doi:10.1097/00006123-200109000-00027

Vanlandewijck M, He L, Mae MA, Andrae J, Ando K, Del Gaudio F, Nahar K, Lebouvier T, Lavina B, Gouveia L, Sun Y, Raschperger E, Rasanen M, Zarb Y, Mochizuki N, Keller A, Lendahl U, Betsholtz C (2018) A molecular atlas of cell types and zonation in the brain vasculature. Nature 554 (7693):475-480. doi:10.1038/nature25739

Wang J, Vasaikar S, Shi Z, Greer M, Zhang B (2017) WebGestalt 2017: a more comprehensive, powerful, flexible and interactive gene set enrichment analysis toolkit. Nucleic Acids Res 45 (W1):W130-W137. doi:10.1093/nar/gkx356

Yu Y, Cai Z, Cui M, Nie P, Sun Z, Sun S, Chu S, Wang X, Hu L, Yi J, Shen L, He B (2015) The orphan nuclear receptor Nur77 inhibits low shear stress-induced carotid artery remodeling in mice. Int J Mol Med 36 (6):1547-1555. doi:10.3892/ijmm.2015.2375

Zehendner CM, Tsohataridis S, Luhmann HJ, Yang JW (2013) Developmental switch in neurovascular coupling in the immature rodent barrel cortex. PLoS One 8 (11):e80749. doi:10.1371/journal.pone.0080749

Zheng M, Cheng H, Banerjee I, Chen J (2010) ALP/Enigma PDZ-LIM domain proteins in the heart. J Mol Cell Biol 2 (2):96-102. doi:10.1093/jmcb/mjp038

Figure legends

Fig. 1 Brain MVs follow a transcriptional maturation program between P5 and P15

A. Flowchart of the transcriptional analysis of MVs extracted from dorsal cortex on P5 and P15. Endothelial cells are represented in red, pericytes in yellow, vascular smooth muscle cells in blue and fibroblasts in green. **B.** Ratio of qPCR quantification for the pericyte-specific transcripts *Abcc9* and *Kncj8* on the endothelial specific transcript *Pecam1* in MVs and cortex on P5 and P15. The plotted data are quoted as the mean ± SD. Two-tailed Mann-Whitney test (n=4 samples per stage; number of mice per MV sample: 3 for P5; 3 for P15; One mouse per dorsal cortex sample). Data are given in **Table S4**. **C.** Hierarchical clustering heat map of the RNAseq analysis of dorsal cortical MVs on P5 and P15. n=3 libraries for each stage. **D.** Volcano plot of the RNAseq results for the 11286 transcripts with more than 50 reads in at least one stage. Each transcript is represented by a dot. The threshold for a transcriptional change is p-value < 0.05 (horizontal dotted line) and Log2 fold change (FC) > 1 or < -1 (vertical dotted lines). Transcripts with no changes (1 < log2FC < 1 or padj > 0.05) are in grey; transcripts upregulated on P15 (padj ≤ 0.05; transcripts: log2FC ≥ 1) are in red; transcripts downregulated on P15 (log2FC ≤ -1, padj ≤ 0.05) are in blue. **E.** A REViGO representation of gene ontology (GO) analysis of transcriptional changes in cortical MVs between P5 and P15 for "biological processes". Data are given in **Table S2**.

Fig. 2 Identification of the transcriptional signature of brain vascular cells and characterization of their postnatal expression within MVs

A. Flowchart of the identification of cell-type-specific or -preferentially expressed transcripts from the vascular single cell database (He et al. 2016; Vanlandewijck et al. 2018) and study of their expression in our transcriptional analysis of MVs extracted from dorsal cortex on P5 and P15. Endothelial cells are represented in red, pericytes in yellow, vascular smooth muscle cells in blue and fibroblasts in green**. B.** log2FC for cell-type-specific or -preferentially expressed transcripts in cortical MVs on P5 and P15. Each dot represents a transcript. Red dots correspond to significant changes between P5 and P15 (log2FC ≤ -1 or log2FC ≥ 1, padj ≤ 0.05). Black dots correspond to transcripts that did not change between P5 and P15 (-1 < log2FC <1 or padj > 0.05). Lines indicate the mean for each category. **C.** RNAseq data for significantly changed VSMC-preferentially expressed transcripts in cortical MVs between P5 and P15. Data are given in **Table S3**.

Fig. 3 Validation of transcriptional maturation in arteriolar VSMCs from P5 to P15

A. qPCR results for vascular smooth muscle cell-specific or -preferentially expressed transcripts on P5, P10 and P15 purified MVs from whole brain are shown. Signals were normalized against *Gapdh*. The value on P5 was set to 1 (dotted line). The plotted data are quoted as the mean ± SD. Kruskal-Wallis test (overall, in bold) and one-tailed Mann-Whitney test (comparison of stages) for 3 to 5 samples per stage (mice per sample: 5 for P5; 3 for P15; 2 for P30; 2 for P60). **B-F.** FISH analysis of Myh11 expression on P5 and P15. Confocal microscopy images (FISH detection) of *Myh11* mRNAs (red dots) in the cortex (**B**) or in purified MVs (**C**). Vessels were stained with isolectin B4 (IB4). Nuclei were stained with Hoechst. White arrowheads indicate FISH dots in vascular smooth muscle cells. **D-F.** Quantification. **D.** Dot plot representation of the analyzed purified MV diameter on P5 and P15. Red lines indicate mean ± SD values (284 vessels at P5 and 313 vessels at P15 from 3 independent MV preparations). Two-tailed Mann-Whitney test. **E.** MVs were divided into three categories, according to their FISH dot density. The proportion of MVs in each category on P5 and P15 are shown. A chi² test for changes in the distribution across vessel categories (bold) and a one-tailed Mann-Whitney test for changes over time of each category (284 vessels at P5 and 313 vessels at P15 from 3 independent MV preparations). **F.** MV diameter for each FISH dot density category on P15. Kruskal-Wallis test (overall, in bold) and a one-tailed Mann-Whitney test (comparison of categories) (330 vessels from 3 independent MV preparations). Data are given in **Table S4**.

Fig. 4 Postnatal acquisition of VSMC contractile molecular properties and expansion of the VSMC contractile network

A. Western blot detection and analysis of SMA, Myh11 and histone 3 (H3) in protein extracts from MVs purified from whole brain on P5, P15, P30 and P60. Signals were normalized against H3. The results on P5 were set to 1. Kruskal-Wallis test (overall, in bold) and a one-tailed Mann-Whitney test (comparison of stages). The data are quoted as the mean ± SD (n = 3 or 4 samples per developmental stage; mice per sample: 5 for P5; 4 for P10; 3 for P15; 2 for P60). **B. C.** Representative 3D images of the arterial network in cleared brains and (at higher magnification) in the dorsal part of the somatosensory cortex on P5, P15 and P60, after immunolabeling for SMA (**B, C**) and Pecam-1 (**C**). **D.** Comparative analysis of the SMA-positive vessel length, number of primary or total branches, and ramification in the parenchymal cortex. The data are quoted as the mean ± SD (n = 3 mice per stage). Kruskal-Wallis test (overall, in bold) and a one-tailed Mann-Whitney test (comparison of stages). Data are given in **Table S4**.

Fig. 5 VSMC contractility and CBF mature postnatally in the mouse cortex with heterogenous developmental trajectories within cortical regions.

A-C. *Ex vivo* analysis of arteriolar constriction on slices of somatosensory cortex from mice on P5, P15 and P60. **A.** Representative infrared images of arteriole constriction in response to bath application of U46619 and dilation upon washing, for samples obtained on P5 and P60. The vessel lumen is indicated by a red dotted line. **B.** Time course of the change in vessel lumen size for P5, P15 and P60 samples. 0 min corresponds to the addition of U46619 in the recording chamber medium. The data are quoted as the mean ± SEM. **C.** Analysis of **(B)**. Maximal amplitude and slope of the contraction. The mean value before U466619 application was set as 0. Kruskal-Wallis test (overall, in bold) and a one-tailed Mann-Whitney test (comparison of stages). The data are quoted as the mean ± SD (n = 13 vessels on P5; 9 on P15; 8 at P60; 3 mice per group). **D.** Quantification of vessel diameter before U46619 application. The data are quoted as the mean ± SD. (n = 13 vessels on P5; 9 on P15; 8 at P60; 3 mice per group). **E.** qPCR results for *Tbxa2r* in mRNAs from MVs purified from whole brain on P5, P15 and P60. Signals were normalized against *Gapdh*. The results on P5 were set to 1. Kruskal-Wallis test (overall, in bold) and a one-tailed Mann-Whitney test (comparison of stages). The data are quoted as the mean ± SD. n= 3 to 5 samples per stage (mice per sample: 5 for P5; 3 for P15; 2 for P30; 2 for P60). **F. G.** *In vivo* analysis of the CBF by ASL MRI from mice on P5, P15 and P30. **F.** Representative T2 (up) and ASL (down) MRI images. Boxed areas indicate dorsal and lateral cortical areas. **G.** Analysis of the CBF in the whole cortex (left); dorsal/lateral CBF ratio (right). The data are quoted as the mean ± SD. One-way ANOVA (overall, in bold) and Tukey's multiple comparison test (comparison of stages) (n= 9 or 10 mice per group). **H**. Representative 3D images of the arterial network in cleared brains with a focus on the dorsal and lateral parts of the cortex on P15 after immunolabeling for SMA. Images 1 and 2 are enlarged views of white boxes **I.** Comparative analysis of the SMA-positive vessel length, number of primary or total branches, and ramification in the parenchymal cortex. The data are quoted as the mean ± SD (n = 3 hemispheres; 2 mice). One-tailed Mann-Whitney test. **J.K.** Western blot detection and analysis of SMA and histone 3 (H3) in protein extracts from MVs purified from dorsal and lateral parts of the cortex on P15. Signals were normalized against H3. **K.** Analysis of (**J**). The data are quoted as the mean ± SD (n = 4 samples per brain area; each sample is a pool of MVs purified from 4 mice). The results on dorsal MVs were set to 1. One-tailed Mann-Whitney test. Data are given in **Table S4**.

Fig. 6 The network of contractile VSMCs matures postnatally in the human cortex

A. B. Immunohistochemistry analysis of MYH11 (**A**) and SMA (**B**) expression in the developing human cortex. Representative images of MYH11 (**A**) or SMA (**B**) –immunostained brain cortical slices (left) and (at higher magnification) in the parenchyma of the boxed area (right) for samples taken (i) in the prenatal period (15 wg to 39 wg), (ii) between 0 and 2 years of age, (iii) between 2 and 5 years of age and (iv) after 10 years of age. Expression in penetrating arterioles (arrow) and parenchymal arterioles (arrowheads) was revealed by DAB staining. **C. D.** Quantification of the MYH11- (**C**) or SMA- (**D**) stained surface areas and the number of detected objects, quoted as the mean ± SD. Kruskal-Wallis test (overall, in bold) and one-tailed Mann-Whitney test (comparison of stages). Number of samples per developmental age: 5 or 6 for prenatal, 4 for 0-2 years, 4 for 2-5 years and 7 or 8 for >10 years (see details in Materials and Methods). Data are given in **Table S4**.

Supplemental information

Table S1 Dataset of the comparison of cortical MV transcriptomes on P5 and P15

Selected mRNAs have a mean number of reads ≥ 50 in at least one condition. The fold-change (FC) between expression on P5 and P15 and associated adjusted p-values (padj) are indicated. Base mean: mean reads for each transcript. n=3 libraries for each stage.

Table S2 Gene ontology data sets

In cortical MVs, the "biological process" and "cellular component" GO pathways significantly changed between P5 and P15.

Table S3 Identification of vascular-cell-type-specific or -preferentially expressed transcripts

Cell-type-specific or -preferentially expressed transcripts are listed for each cluster. Left-hand columns: identification of transcripts -preferentially expressed in or specific to each cell. Middle columns: % of single-cells within and outside each cluster expressing the transcript logFC of expression difference between cells of the cluster and outside and the associated adjusted p-values. Right-hand columns: cortical MV RNA-Seq analysis. Log2FC on P15 versus P5 and the associated adjusted p-values. EC, endothelial cell; PC, pericyte; FB, fibroblast: VSMC, vascular smooth muscle cell.

Table S4 Datasets

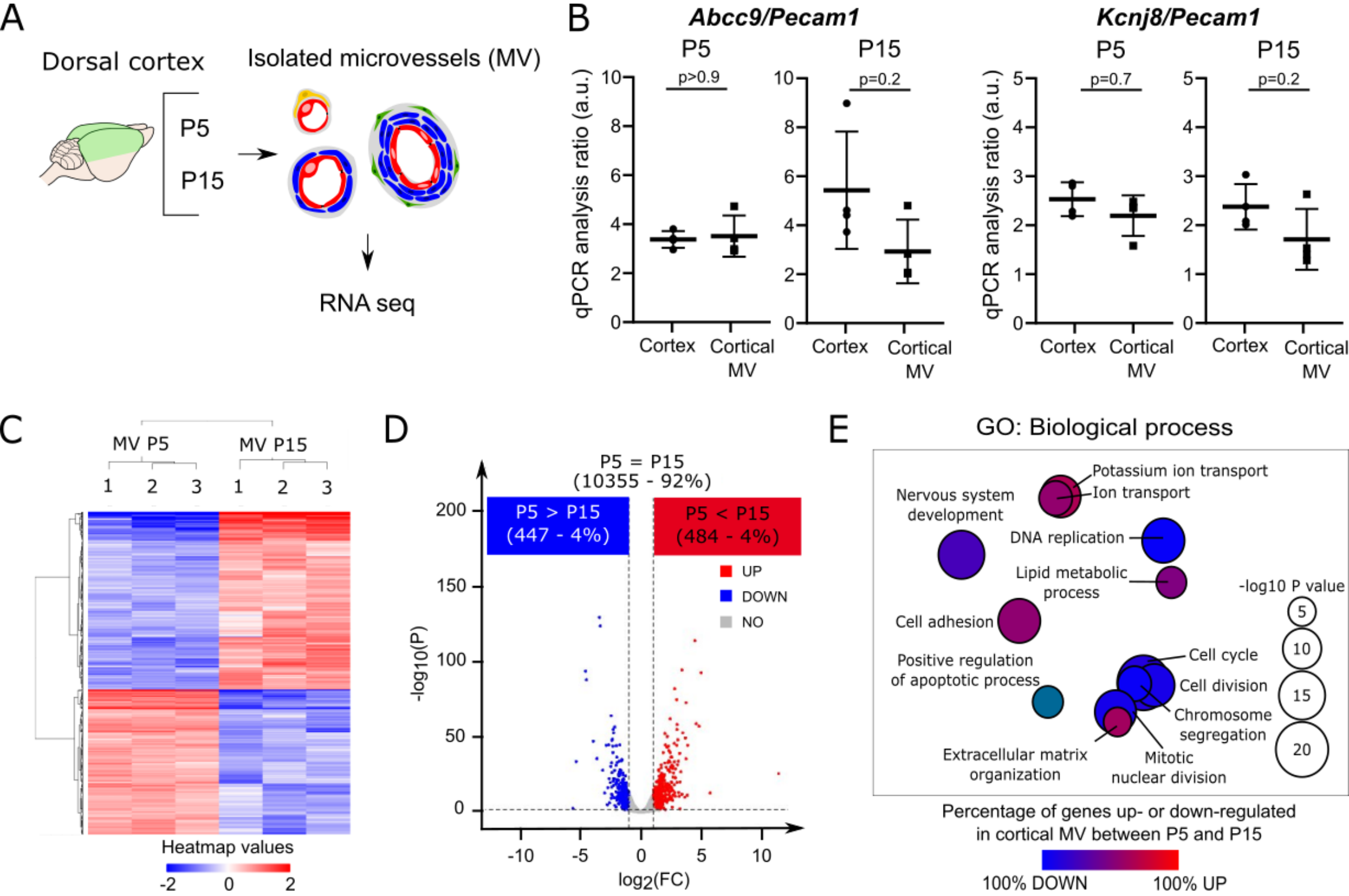
A
Dorsal cortex
Isolated microvessels (MV)
P5
P15
RNA seq
B
Abcc9/Pecam1
Kcnj8/Pecam1
P5
P15
p>0.9
p=0.2
p=0.7
qPCR analysis ratio (a.u.)
Cortex
Cortical MV
C
MV P5
MV P15
1 2 3 1 2 3
Heatmap values
-2 0 2
D
P5 = P15
(10355 - 92%)
P5 > P15
(447 - 4%)
P5 < P15
(484 - 4%)
UP
DOWN
NO
-log10(P)
log2(FC)
E
GO: Biological process
Potassium ion transport
Ion transport
Nervous system development
DNA replication
Lipid metabolic process
Cell adhesion
Positive regulation of apoptotic process
Cell cycle
Cell division
Chromosome segregation
Extracellular matrix organization
Mitotic nuclear division
-log10 P value
Percentage of genes up- or down-regulated in cortical MV between P5 and P15
100% DOWN
100% UP

A

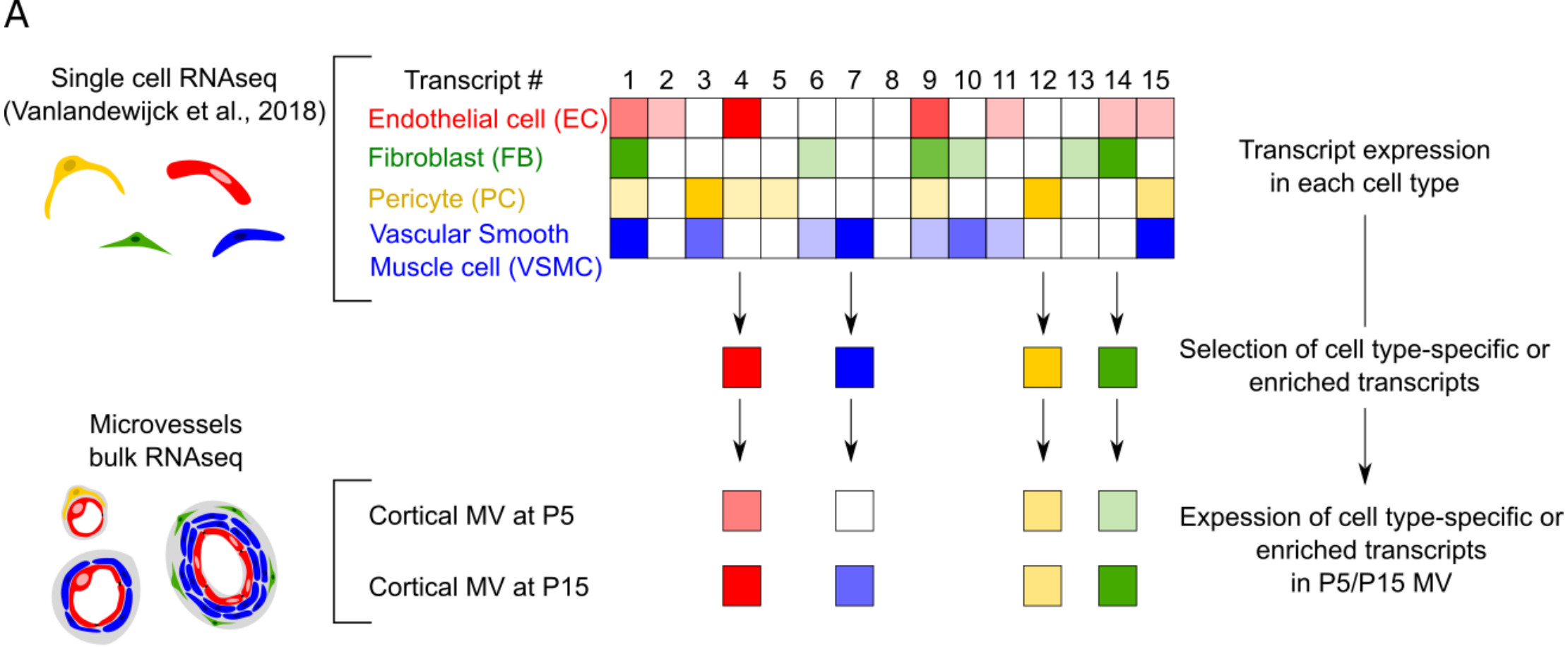

B

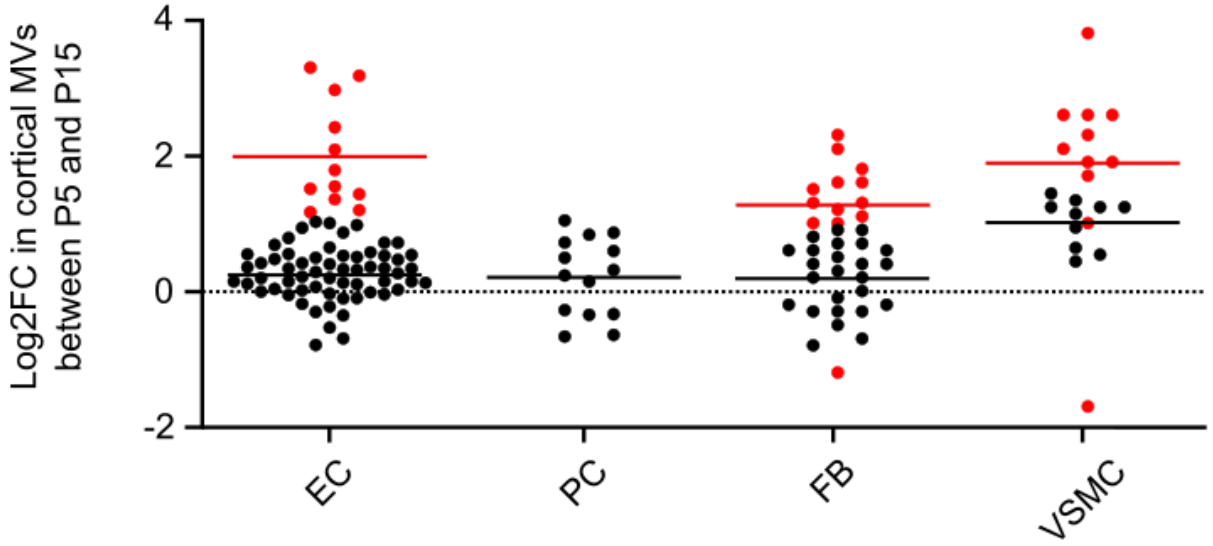

C

Cluster	Gene	RPKM MV P5	RPKM MV P15	P5 vs P15 log2FC	P5 vs P15 AdjP-value
VSMC	*Pdlim3*	0,2	3,3	3,8	9,6E-12
	Acta2	29,4	182,3	2,6	2,9E-08
	Myh11	2,3	14,0	2,6	1,1E-03
	Tagln	4,0	23,9	2,6	8,3E-32
	Nr4a1	8,2	41,0	2,3	2,1E-28
	Mustn1	1,9	8,3	2,1	1,7E-17
	Nrip2	4,4	17,1	1,9	3,8E-17
	Ltbp1	1,2	4,3	1,9	1,1E-07
	Tpm2	16,2	53,6	1,7	6,2E-15
	Pln	2,1	4,5	1,0	9,0E-06
	Map1b	61,6	18,5	-1,7	1,2E-28

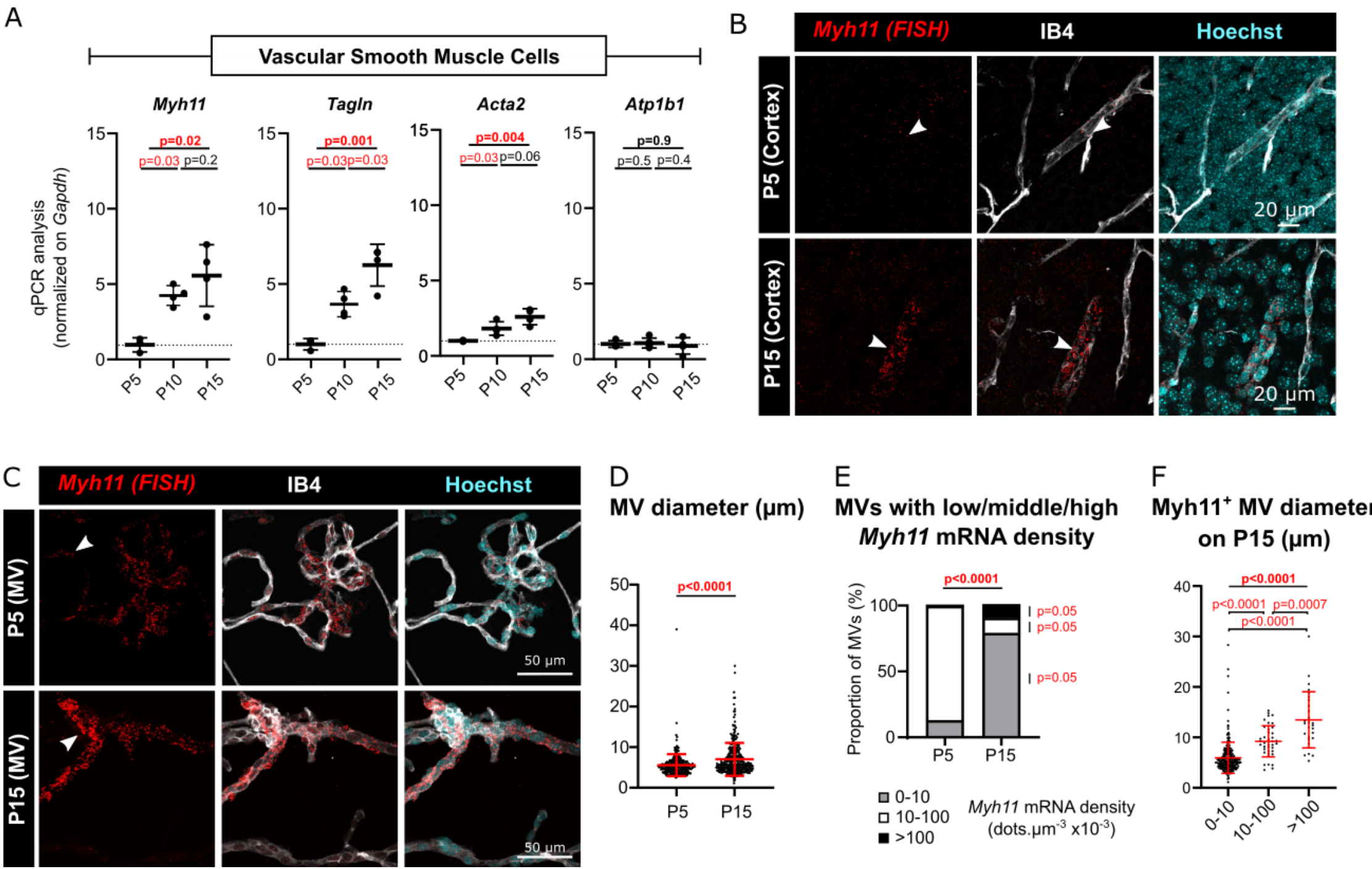
A
Vascular Smooth Muscle Cells
Myh11
Tagln
Acta2
Atp1b1
qPCR analysis (normalized on Gapdh)
p=0.02
p=0.03 p=0.2
p=0.001
p=0.03 p=0.03
p=0.004
p=0.03 p=0.06
p=0.9
p=0.5 p=0.4
P5
P10
P15
B
Myh11 (FISH)
IB4
Hoechst
P5 (Cortex)
P15 (Cortex)
20 µm
C
Myh11 (FISH)
IB4
Hoechst
P5 (MV)
P15 (MV)
50 µm
D
MV diameter (µm)
p<0.0001
E
MVs with low/middle/high Myh11 mRNA density
p<0.0001
Proportion of MVs (%)
p=0.05
p=0.05
p=0.05
0-10
10-100
>100
Myh11 mRNA density (dots.µm-3 x10-3)
F
Myh11+ MV diameter on P15 (µm)
p<0.0001
p<0.0001 p=0.0007
p<0.0001
0-10
10-100
>100

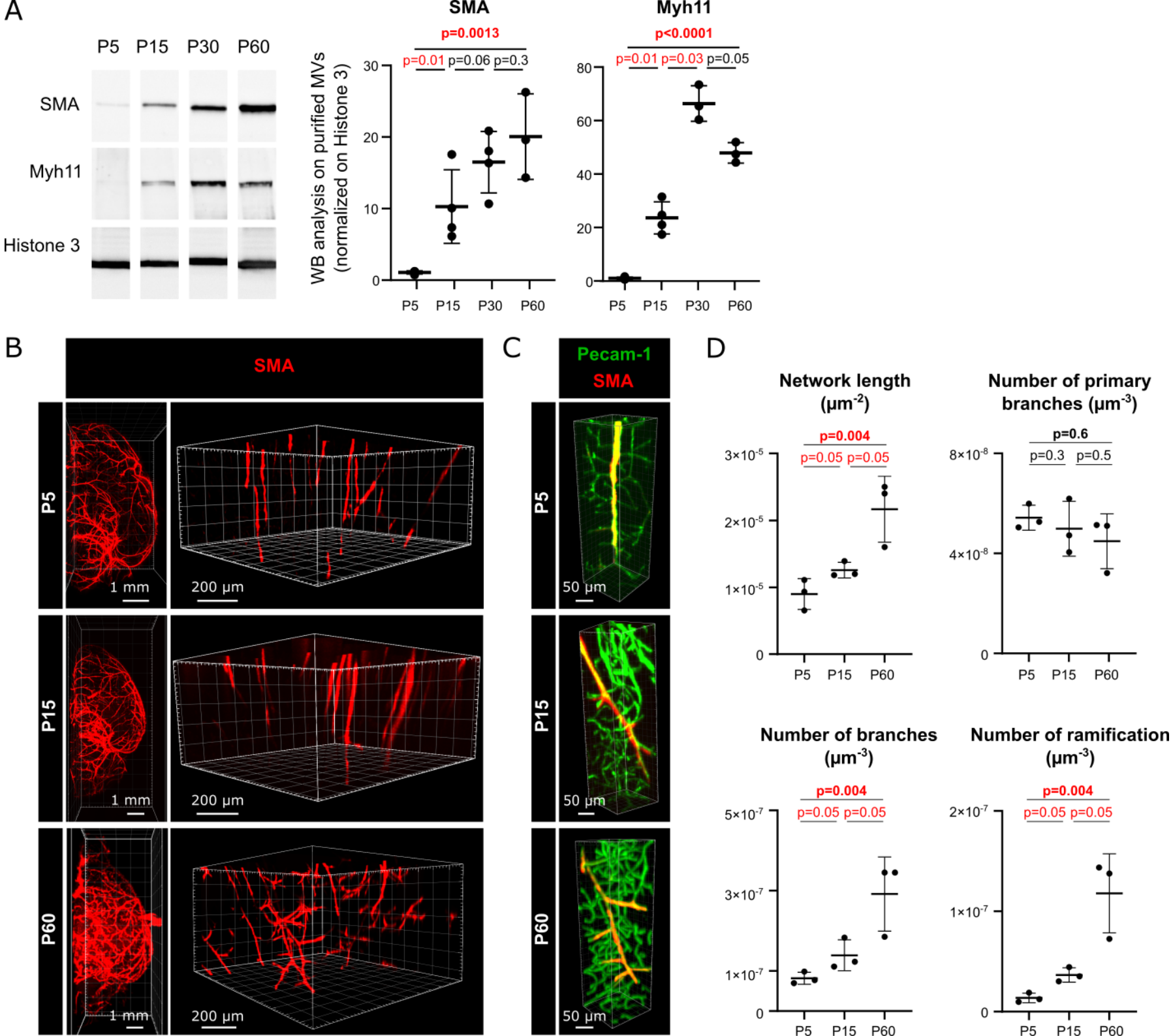
A
P5 P15 P30 P60
SMA
Myh11
Histone 3
WB analysis on purified MVs (normalized on Histone 3)
SMA
p=0.0013
p=0.01 p=0.06 p=0.3
Myh11
p<0.0001
p=0.01 p=0.03 p=0.05
B
SMA
P5
P15
P60
1 mm
200 µm
C
Pecam-1
SMA
50 µm
D
Network length (µm-2)
p=0.004
p=0.05 p=0.05
Number of primary branches (µm-3)
p=0.6
p=0.3 p=0.5
Number of branches (µm-3)
p=0.004
p=0.05 p=0.05
Number of ramification (µm-3)
p=0.004
p=0.05 p=0.05

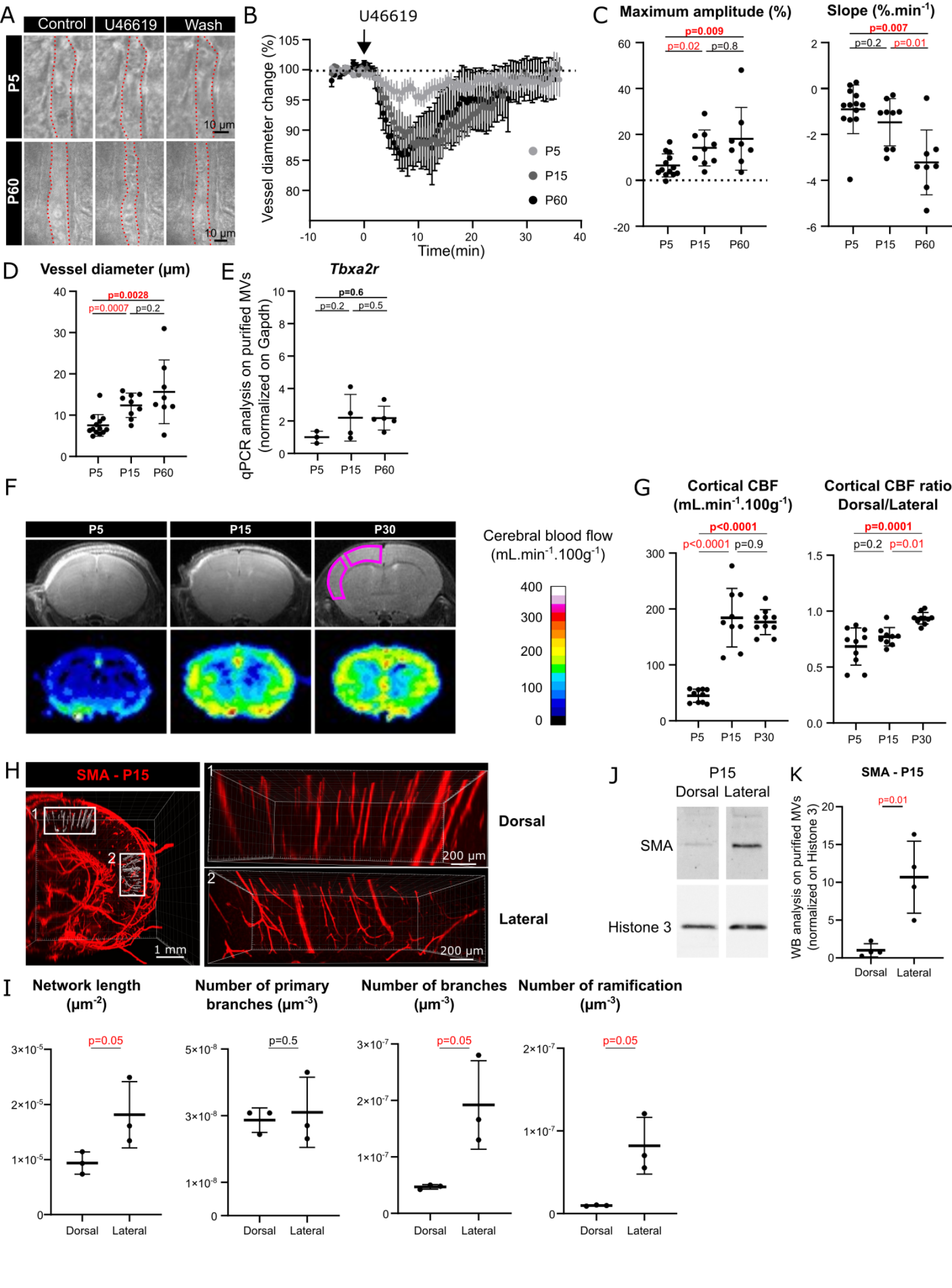
A
Control
U46619
Wash
P5
P60
10 µm
B
U46619
Vessel diameter change (%)
Time(min)
P5
P15
P60
C
Maximum amplitude (%)
p=0.009
p=0.02
p=0.8
Slope (%.min-1)
p=0.007
p=0.2
p=0.01
D
Vessel diameter (µm)
p=0.0028
p=0.0007
p=0.2
E
Tbxa2r
qPCR analysis on purified MVs (normalized on Gapdh)
p=0.6
p=0.2
p=0.5
F
P5
P15
P30
Cerebral blood flow (mL.min-1.100g-1)
G
Cortical CBF (mL.min-1.100g-1)
p<0.0001
p<0.0001
p=0.9
Cortical CBF ratio Dorsal/Lateral
p=0.0001
p=0.2
p=0.01
H
SMA - P15
1 mm
200 µm
Dorsal
Lateral
J
P15
Dorsal Lateral
SMA
Histone 3
K
SMA - P15
WB analysis on purified MVs (normalized on Histone 3)
p=0.01
I
Network length (µm-2)
p=0.05
Number of primary branches (µm-3)
p=0.5
Number of branches (µm-3)
p=0.05
Number of ramification (µm-3)
p=0.05

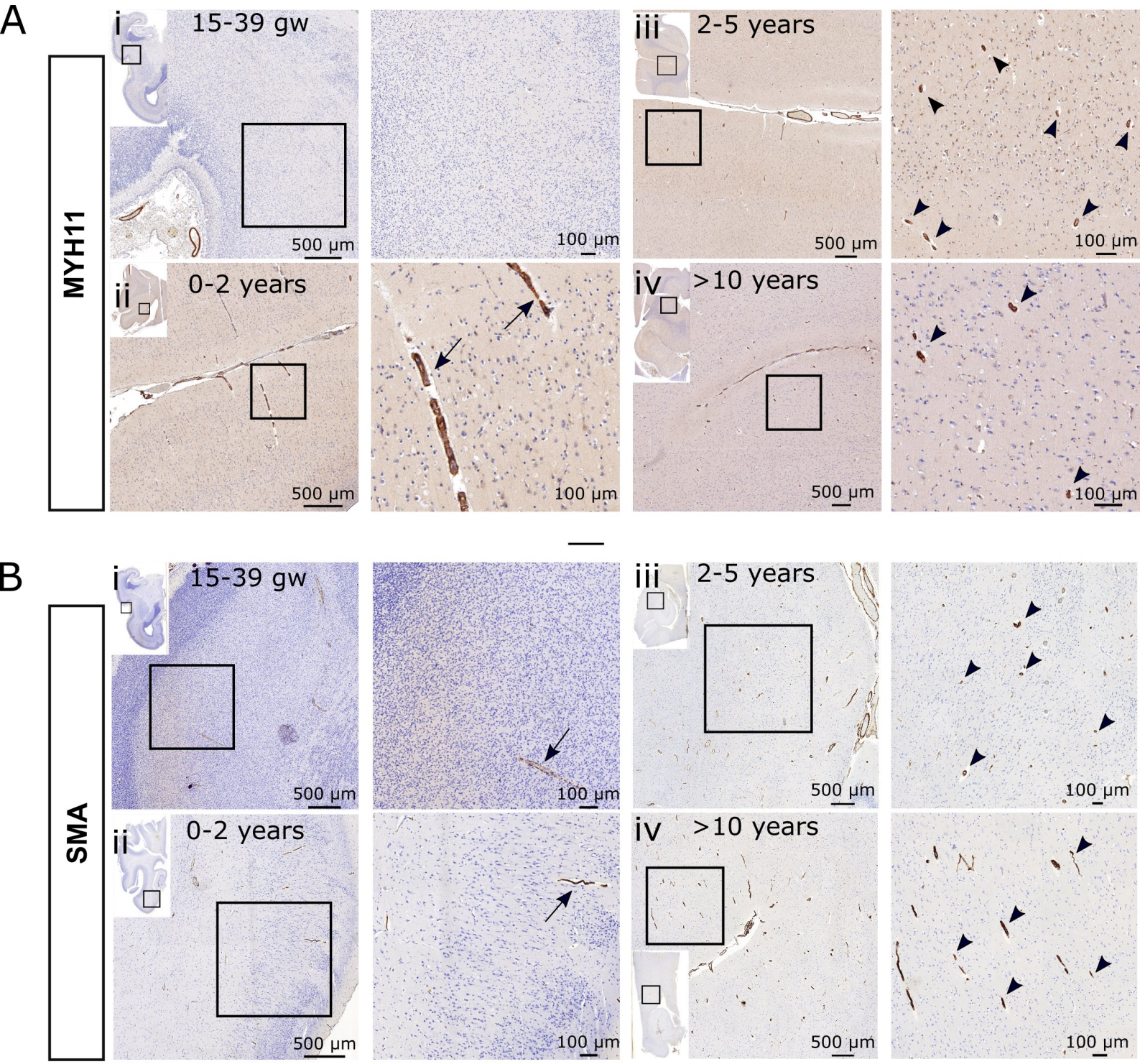
A
MYH11
i
15-39 gw
500 µm
100 µm
ii
0-2 years
500 µm
100 µm
iii
2-5 years
500 µm
100 µm
iv
>10 years
500 µm
100 µm
B
SMA
i
15-39 gw
500 µm
100 µm
ii
0-2 years
500 µm
100 µm
iii
2-5 years
500 µm
100 µm
iv
>10 years
500 µm
100 µm

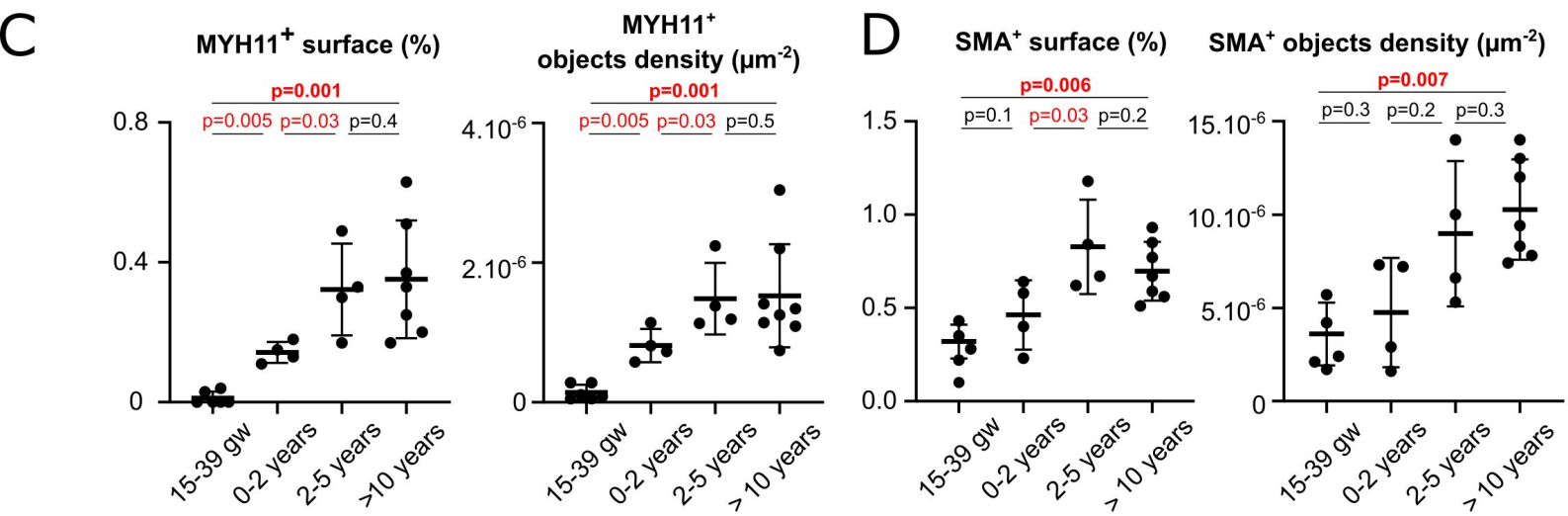
C
MYH11+ surface (%)
p=0.001
p=0.005 p=0.03 p=0.4
0.8
0.4
0
MYH11+ objects density (µm-2)
p=0.001
p=0.005 p=0.03 p=0.5
4.10-6
2.10-6
0
15-39 gw
0-2 years
2-5 years
>10 years
D
SMA+ surface (%)
p=0.006
p=0.1 p=0.03 p=0.2
1.5
1.0
0.5
0.0
SMA+ objects density (µm-2)
p=0.007
p=0.3 p=0.2 p=0.3
15.10-6
10.10-6
5.10-6
0
15-39 gw
0-2 years
2-5 years
> 10 years